# HEXAGONAL VS PINWHEEL SEGMENTED TELESCOPES: A COMPARISON STUDY OF DEGRADED POINT-SPREAD-FUNCTIONS FROM RANDOM TIP-TILT AND PISTON MISALIGNMENT OF SEGMENTS

by

Charles J. Taylor



A Report Submitted to the Faculty of the

COLLEGE OF OPTICAL SCIENCES

In Partial Fulfillment of the Requirements

For the Degree of

MASTER OF OPTICAL SCIENCES

In the Graduate College

THE UNIVERSITY OF ARIZONA

2023

THE UNIVERSITY OF ARIZONA
GRADUATE COLLEGE

As members of the Master's Committee, we certify that we have read the thesis prepared by Charles J. Taylor, titled Hexagonal vs Pinwheel Segmented Telescopes: A Comparison Study of Degraded Point-Spread-Functions from Random Tip-Tilt and Piston Misalignment of Segments and recommend that it be accepted as fulfilling the dissertation requirement for the Master's Degree.

_____ Date: _____
*Dr. Daewook Kim*

_____ Date: _____
*Dr. Yuzuru Takashima*

_____ Date: _____
*Dr. Heejoo Choi*

Final approval and acceptance of this report is contingent upon the candidate's submission of the final copies of the report to the Graduate College.

I hereby certify that I have read this report prepared under my direction and recommend that it be accepted as fulfilling the Master's requirement.

_____ Date: _____
*Dr. Daewook Kim*
Master's Thesis Committee Chair
*College of Optical Sciences*

## ACKNOWLEDGMENTS

Katlyn Taylor: My beautiful wife, thank you for your endless support through the long nights and early mornings. When I started this journey for a Master's we were only engaged. At the end of this we are married and have two beautiful baby girls. One of which was born, 1 week before my defense in Tucson. I love you and am so grateful for our beautiful family.

Dr. Daewook Kim: Thank you for accepting me into the LOFT family and being so supportive of my schedule. Additionally, your positivity and love for Optics is infectious and I am grateful for your guidance and friendship.

Dr. Yuzuru Takashima: Thank you for accepting the role as a committee member and your insightful and detailed questions throughout.

Dr. Heejoo Choi: Thank you for accepting the role as a committee member and your assistance along the way.

PhD Candidate Kevin Derby: Thank you for all of your help and collaboration. You were paramount to my success. I am grateful for your time and friendship.

# TABLE OF CONTENTS

# LIST OF FIGURES

# LIST OF TABLES

## ABSTRACT

Future telescopes will need larger primary mirrors. A way to reduce cost, manufacturing difficulties and transportability is to segment the primary mirror. The next thing to consider is the geometry of the segments. The James Webb Space Telescope produced Hexagonal shaped segments. This configuration has benefits, however there are some imaging limitations introduced by the high frequency components due to the edges of the segments. The edges of the segments behave like a 2-D diffraction grating. The sharp edges and points of the hexagonal segment create the higher order frequencies that contribute to the spikes in the point-spread-function that prohibit view of other interesting objects like exoplanet research [6,8]. A Pinwheel segmented aperture enables the view of these objects by dispersing the energy in the spikes [8,10]. The structure that supports the segments will inevitably have misalignment errors attributed. This paper will partially analyze the inevitable misalignment errors of Piston, and Tip/Tilt. It is the goal of this paper to determine which segmented mirror is less sensitive to misalignment errors.


## 1. INTRODUCTION

Segmented mirror technology enables production of large telescope designs, which allows a deeper and further study of the universe. This paper will attempt to determine which segmented mirror, Hexagonal or Pinwheel, is less sensitive to segment misalignment evaluated by analyzing the degraded point-spread-functions (PSF). It is assumed the Pinwheel Aperture will be less sensitive. This assumption is based off the behavior of the curved segments that fan out the energy from diffraction features [8,10]. The flow of this paper will begin with a literature review and motivation for this study. The next topic will derive some of the diffraction equations used to calculate the PSF, which is the main output from the simulation. The simulation is done in HCIPy, which is covered in detail below. HCIPy is used to create the two aperture types, with the intention to make the segments and overall aperture topology as similar as possible. HCIPy is used to apply the segment misalignment. A verification is done to ensure the PSF's simulations are behaving as expected. HCIPy outputs raw PSF images, that are imported into Matlab.

Matlab is used to extract and analyze each PSF. The merit of quality used here is the Encircled Energy Radius (EER) and the Strehl Ratio. The remainder of the paper is used to analyze and produce a direct comparison using a Monte Carlo of 10 data runs. The final goal of this paper is to prove the Pinwheel Segmented Aperture is less sensitive to segment Misalignment errors when directly compared to the Hexagonal Segmented Aperture.

## 2. LITERATURE REVIEW

### 2.1. History of the Telescope

Before the modern-day city lights polluted the night sky, interested parties would gaze upon the heaven's bright and beautiful stars possessed only with the tool of the naked eye. Once the ability to magnify distant objects was realized, presumably by Dutch spectacle makers, the technology grew popularity in navigational and military applications. In 1609, Galileo Gallie was among the first to advance the field of astronomy by pointing his simple two lens, refractive telescope at the sky [3]. The first telescopes were riddled with spherical and chromatic aberrations [1]. It is easier to manufacture a spherically shaped lens, which focuses rays as a function of the lens diameter. The larger diameter of the spherical lens, the more spherical aberration will be present, with exception of an aplanatic element. The simple spectacle lenses used in the first telescopes were made from a single index of refraction, which disperses the wavelengths causing chromatic aberrations. It was eventually realized by looking at the human eye, which contains multiple different materials, and thus indices of refraction could be the solution for solving the chromatic aberrations [1]. Most telescopes of the time were not reflective, mirrors were a difficult resource and most would have to construct their own. The first reported telescope containing a mirror was from Niccolo Zucchi in his 1616. The first reflecting telescopes using mirrors controlled the chromatic imaging issues by using alloyed metal, however the spherical aberrations were not practically solved until 1636 by Marin Mersenne, who made use of a parabolic mirror. Shortly after James Gregory built upon Mersenne and used geometry to derive an experiment where the shape of the

primary mirror was concave parabolic accompanied by a secondary concave ellipsoidal mirror that directed the light back through a hole in the primary mirror, similar to the Ricthey-Chretien [1]. At the eye-piece the image was chromatically and spherically corrected.

### 2.2. Motivation for Large Telescopes

Eventually, telescope imaging no longer needed a human viewer. Additionally, the need for clearer skies to view the cosmos led to the motivation for space telescopes. As sights began to extend further from our home the need for large space telescopes became evident to answer more exciting questions about the universe and its beginning. Currently, physical laws prohibit scientific expeditions to distant galaxies due to the accelerating expansion of the universe. If humans did leave Earth, it is likely they would never reach outside the Milky Way. Therefore, telescopes are instrumental for viewing the far reaches of the universe, answering fundamental questions about the universe, its origins, and questions about extraterrestrial life. In order to maximize the ability to distinguish two distant objects, known as the Rayleigh Criterion of resolution, the primary mirror needs to be large. The minimum resolvable separation is proportional to wavelength divided by the entrance pupil diameter, $\frac{\lambda}{D}$ , as the Diameter of the entrance pupil grows the resolvable separation decreases and two spatially close distant objects are resolvable [2]. However, angular resolution is not the only reason larger primary mirrors are desirable in future telescope designs. Most objects of interest to astronomers are extremely dim. This can be solved by integrating the sensor over long periods of time, or maximizing the light collecting onto the detectors. Before Adaptive Optics, terrestrial telescopes were noise limited. To increase the signal to noise ratio, which goes like $\frac{1}{D^2}$ , where $D$ is the diameter of the entrance pupil, a larger mirror was necessary. Now, using Adaptive Optics techniques the terrestrial telescope systems are diffraction-limited [3].

### 2.3. Space Telescopes and Segmentation

The Hubble Space Telescope launched by NASA in 1990 has been the single most productive data collecting instrument ever deployed. Over 15,000 scientific papers published in 20 years [1]. Terrestrial based telescopes located even in the best atmospheric conditions are still limited to the particles in the atmosphere that absorb bands of electro-magnetic energy, leaving holes in the wavelength spectrum that are collectable. The Hubble Space Telescope was initially designed to contain a 3-meter primary mirror in a Ricthey-Chretien optical train. However, congress cut funding and forced the design to be decreased to a 2.4-meter hyperbolic primary mirror, which still allowed for a monolithic mirror to be manufactured and launched [1]. In 1989, Nasa began planning the Next Generation Space Telescope (NGST), known now to be the James Webb Space Telescope (JWST). A study in 1996 determined a primary mirror of 8-meters was necessary to meet the program requirements for the NGST [4]. The launch compartment is only 4.5-meters. Not only is an 8-meter monolithic mirror incredibly expensive and complicated to manufacture, the only way to fit an 8-meter mirror into a 4.5-meter vehicle is to segment it, fold it. Future astronomical telescopes will have segmented primary mirrors [6]. After many years of technology development and opto-mechanical nightmares, the JWST was launched with 18 Hexagonal shaped segments that form a 6.5-meter primary collecting aperture. However, JWST is not the first reported use of segmented primary mirror being used in a telescope design. There are reports of Archimedes in 212 BC using segmented optics in an array of mirrors to focus the suns light onto attacking Roman ships [3]. More recently, in 1932 Horn d'Arturo of Italy used 61 Hexagonal segments to form a 1.5-meter mirror [3]. More recently, there are telescope designs that propose primary mirrors containing around 3300 segments. Studies of manufacturing and transportation issues of large primary mirrors have concluded that hexagonally shaped segments are the optimal design [6].

### 2.4. Segmentation Diffraction Effects

Although segmented primary mirrors allow telescopes to scale with size, even the best actively aligned segments will degrade image quality compared to a design with less segmented optics. Even the slightest misalignment of the segments, which is inevitable, cause the primary mirrors to act like a giant 2-D blazed grating, which produce diffraction effects that appear as regular periodic interference patterns on the sensor [6]. These effects may be small compared to the bright object, however, there are cases in which these diffraction effects cloud out dim objects that are of interest. Consider the research for Earth-like planets, which are $10^{-9}$ less bright than their orbiting star [6]. Mechanical limitations of the segments support structure inevitably produce Piston and Tip-Tilt errors. An analytical description of the PSF for segmented apertures with misalignment errors is complicated, however has been done [6]. The PSF of an ideal segmented mirror is represented as the convolution of two terms. The first factor is the grid-function, which is the Fourier Transform of the segmentation geometry grid that is seen as a periodic function of sharp peaks, each of which is the Fourier transform of the full telescope diameter [9]. The second is the PSF of an individual segment [6]. The presence of Piston errors does not change the individual segment PSF, however these errors do modify the grid-function [6]. Each segment produces its own PSF which is stacked spatially concentric with respect to the center energy spot, but out of phase, which degrades high-order frequencies, and expands the low-order frequencies. The presence of Tip-Tilt errors acts like a randomly blazed 2-D diffraction grating. Each segment tilt shifts the PSF and they are no longer stacked spatially concentric, which degrades all frequencies in the PSF [6]. In other words, a segmented primary mirror can be treated as many individual telescopes corresponding to each segment. The PSF represents a combination of incoherent Intensities from the individual segments, and a coherent term that represents the interference between the individual segments. The PSF observed is combination of N spots, N representing the number of segmented components, reflected by each segment at different angles. As N grows the interference term contributes increasingly to the overall PSF [9]. Other areas of interest for image quality from segmentation fabrication error are gap-size and edge deformation, all of

which can be studied analytically for further communicating technical specifications during manufacturing [6].

### 2.5. Introduction of Hexagonal and Pinwheel Shaped Segments

Studies around improving telescope designs for detection of exoplanets are of interest [8, 9,11]. If the telescope aperture is segmented to produce a discontinuous concave surface, then the gaps will produce diffraction effects across the image. If the gaps are periodic as for many hexagonal geometries, then the diffraction effects produce periodic diffraction effects [11]. In the Hubble Space Telescope, the secondary mirror spiders, structures that support the secondary mirror, introduce diffraction flares, or spikes to the PSF, degrading the spectral data needed for exo-planet research [8]. We have all marveled at the images taken by the Hubble, but it is evident each image of a star contains these four spikes, which does not represent a true image of the object. Werenskiold (1941) was among the first astronomers to suggest the implementation of curved secondary mirror spiders to mitigates these diffraction flares [8]. In a 1984 paper, Richter demonstrated the mitigation effect of using curved secondary mirror spiders using pin-hole diffraction masks illuminated by an incandescent lamp located 13.7 m from the camera [10]. Richter argued that if the entrance pupil was obscured by a precise arc of a circle and each obscuration added to an integer number of circles the diffraction flares, or spikes would be uniformly fanned out into a “searchlight” or “bow tie” effect [8]. There would still be diffraction from the obscurations on the aperture, however there would be no azimuthal periodic spikes to the PSF [8]. For a monolithic circular primary mirror the diffraction-limited image is an Airy Disc pattern. Hexagonally shaped segmented primaries will focus the diffracted energy into line features that are perpendicular to the segment edges, which produces a diffraction-limited image that carries additional bright spikes or flares compared to the Airy Disc [3]. The JWST uses a primary hexagonal segment, and associated PSF contains six of these spikes. The successful alignment of the JWST does not go unnoticed, and its primary mission is to study galaxy formation at the beginning of the universe and the spikes have little impact on this goal. Other studies that involve exo-planet detection and classification are sensitive to these types of diffraction

effects. Therefore, a primary mirror using Pinwheel segmentation, which builds upon secondary mirror spiders, is shown to minimize diffraction flares or spikes [7]. The PSF for a Pinwheel segmented primary mirror is a quasi-Airy Disc.

# 3. BACKGROUND THEORY

## 3.1. PSF Calculation Theory

In general, optical systems usually have limiting apertures, called stops, in which light cannot pass through. More correctly described is that the light interacts with the edges, and the geometric shadow of the aperture is no longer a true shadow, but possess interference effects from the light bending around the corners of the aperture [12]. Diffraction theory is the study of these effects that are not predicted in ray tracing models. There are two approaches to describe diffraction, which are related by Weyl's integral [12]. The first approach is Huygens point-spread-function interpretation where in the aperture the light entering is described as an infinite number of secondary point sources which interfere at the detector. Diffraction, the effects of waves bending around corners, limits the image quality of a sensor. Because of diffraction a point source object being imaged will not be another point source object. Diffraction causes the point to be spread out into a blur spot called the point spread function (PSF) [14]. The diameter of the PSF, assuming the blur spot is circular, is proportional to wavelength divided by the diameter of the stop. Which infers diffraction is worse, bigger blur spot, for longer wavelength or small aperture [14]. Depending on the distance to the detector, approximations can be made to describe the associated PSFs shape, Huygens, spherical, parabolic, or planar, for each point source. The second makes use of the Fourier Transform of the electric field at the aperture multiplied by a transfer function. The result is the Fourier Transform of the electric field at the detector. The transfer function treats diffraction as a linear operation, which propagates the wavefront from aperture to detector [12]. From Green Second Formula, which flows from the Divergence Theorem:

$$\iiint (G\nabla^2 U - U\nabla^2 G)d^3x = \iint \left(G\frac{\partial U}{\partial n} - U\frac{\partial G}{\partial n}\right)d^2x \quad (3.1.1)$$

The equation above relates G and U, which are two continuous scalar functions of position closed within a volume to a surface surrounding the volume [13]. A solution of interest to the Green's Second Formula is the Scalar Helmholtz equation, set equal to zero assumes no U sources inside the volume:

$$(\nabla^2 + k^2)U = 0 \quad (3.1.2)$$

$$(\nabla^2 + k^2)G = \delta(|\vec{r} - \overrightarrow{r_o}|) \quad (3.1.3)$$

In addition, a clever solution for G, in order to constrain Greens Second Formula further, is to substitute G into the Helmholtz equation for U and allow it to equal delta functions that describe point sources inside the volume, in other words G is Greens function, or an impulse response. Here, $k = 2\pi n/\lambda$, where $n$ is the index of refraction, and $\lambda$ is the wavelength. The Helmholtz equation solved for $\nabla^2 U$ and $\nabla^2 G$ are substituted into the left-hand side of Greens Second Formula where the G terms are eliminated leaving a simple sifting property reducing the left-hand side to $-U(\overrightarrow{r_o})$. On the right-hand side, a solution for G is an expanding spherical wave centered on the object. Writing this out becomes the Integral Theorem of Helmholtz and Kirchhoff [12]. A clever solution enforcing G=0 ultimately derives the Rayleigh-Sommerfeld Diffraction Formula, which is the fundamental element for scalar diffraction theory:

$$U_o(\boldsymbol{r}_o) = \int \frac{\left(-\frac{i}{\lambda}+\frac{1}{2\pi r_{o_s}}\right)\gamma_z \exp(ikr_{o_s})}{r_{o_s}} U_s(\boldsymbol{r}_s)d\boldsymbol{r}_s \quad (3.1.4)$$

In the equation above $U_o(\boldsymbol{r}_o)$ describes the Electric Field at the detector or observation point, $U_s(\boldsymbol{r}_s)$ represents the Electric Field of the source in the aperture, $\gamma_z$ is the obliquity factor described as the z-distance from the aperture to the detector divided by $r_{o_s}$, which represents the magnitude of the positive vector from the aperture to the observation point [12].

The Rayleigh-Sommerfeld diffraction formula can be written as $U_s(\boldsymbol{r}_s)$, times the Huygens wavelet assuming the Dirichlet boundary conditions, $h_Z^H(\boldsymbol{r}_o;\boldsymbol{r}_s)$, which is the z-derivative of a spherical wave in the aperture and evaluated at the detector [12].

$$U_o(\boldsymbol{r}_o) = \int U_s(\boldsymbol{r}_s) h_Z^H(\boldsymbol{r}_o;\boldsymbol{r}_s) d\boldsymbol{r}_s \tag{3.1.5}$$

$$h_Z^H(\boldsymbol{r}_o;\boldsymbol{r}_s) = \frac{\left(-\frac{i}{\lambda}+\frac{1}{2\pi r_{o_s}}\right)\gamma_Z \exp(ikr_{o_s}+\emptyset)}{r_{o_s}} \tag{3.1.6}$$

Huygens wavelet is not exactly a spherical wave due to the obliquity factor and phase term, $\emptyset$. The Huygens's wavelet is the most accurate description of an optical system described with scalar diffraction theory.

For distances that are much larger than the wavelengths, it is common to approximate based on the distances that the shape of the incoming wavefronts viewed at the FOV of the detector will have simpler shapes to describe mathematically. Using the Huygens's wavelet we can make approximations to reduce to the Fresnel wavelet. First, when the distance between the aperture and the detector is much larger than the wavelength, $r_{o_s} \gg \lambda$ the $\frac{1}{2\pi r_{o_s}} \to 0$. Second, the obliquity factor is now expanded along with the position term $r_{o_s} = \sqrt{(x_o - x_s)^2 + (y_o - y_s)^2 + z_o^2}$. The first two terms of the Taylor Series expansion for $\sqrt{1+b} \approx 1 + \frac{b}{2} - \frac{b^2}{8}$, are used to approximate $r_{o_s}$ in the exponential. The squared position term in the denominator is substituted for $\frac{1}{r_{o_s}^2} \approx \frac{1}{z_o^2}$. Finally, the Fresnel wavelet then takes the form:

$$h_Z^{Fresnel}(\boldsymbol{r}_o;\boldsymbol{r}_s) = -\frac{iexp(ikz_0)}{\lambda z_0} \exp\left(\frac{ik}{2z_o}[(x_o - x_s)^2 + (y_o - y_s)^2]\right) \tag{3.1.7}$$

When the phase argument of the exponential $\frac{\pi}{\lambda z_o}[(x_o - x_s)^2 + (y_o - x_s)^2]$ set equal to a constant describes parabolic wavefronts [12]. The Fresnel diffraction integral is now:

$$U_o(\boldsymbol{r}_o) = -\frac{iexp(ikz_o)}{\lambda z_o} \int U_s(\boldsymbol{r}_s) \exp\left(\frac{ik}{2z_o}[(x_o - x_s)^2 + (y_o - y_s)^2]\right) d\boldsymbol{r}_s \tag{3.1.8}$$

When the detector is pushed further into the far-field another approximation can be used on the Fresnel wavelet to further reduce the complexity of the incoming wavefronts shape after diffraction from the aperture. The approximations lead to the Fraunhofer wavelet. First, the phase term in the exponential of the Fresnel wavelet is expanded. When $z_o \gg \frac{k}{2}(x_s^2 + y_s^2)$, the of the expanded phase term in the Fresnel wavelet is approximated to unity. The Fraunhofer wavelet takes the form:

$$h_z^{Fraunhofer}(\boldsymbol{r}_o; \boldsymbol{r}_s) = -\frac{iexp(ikz_0)}{\lambda z_0} \exp\left(\frac{-ik}{z_o}[x_o x_s + y_o y_s]\right) \tag{3.1.9}$$

The shape of the incoming wavefronts from each secondary source points within the aperture is planar [12]. This is seen by setting the phase argument of the exponential $-\frac{k}{z_o}[x_o x_s + y_o y_s]$ to be constant. Essentially each wavelet, depending on the distance from the aperture to the detector, is integrated with respect to the aperture plane and provides the full description of the Electric field at the detector. The Fraunhofer Integral becomes:

$$U_o(\boldsymbol{r}_o) = -\frac{iexp(ikz_o)}{\lambda z_o} \int U_s(\boldsymbol{r}_s) \exp\left(\frac{ik}{2z_o}[(x_o - x_s)^2 + (y_o - y_s)^2]\right) d\boldsymbol{r}_s \tag{3.1.10}$$

Analytically integrating the wavelets above can be difficult and rigorous. Using Fourier methods can alleviate these calculations. When the field after the aperture, $U_s^+(x_s, y_s)$ is substituted into the Fresnel diffraction integral and the Fresnel wavelet is expanded it becomes:

$$U_o(\boldsymbol{r}_o) = -\frac{iexp(ikz_o)}{\lambda z_o} \exp\left[\frac{ik}{2z_o}(x_o^2 + y_o^2)\right] \boldsymbol{F}_\xi \boldsymbol{F}_\eta \left\{U_s^+(x_s, y_s) \exp\left[\frac{jk}{2z_o}(x_s^2 + y_s^2)\right]\right\} \tag{3.1.11}$$

$$U_s^+(x_s, y_s) = U_s^-(x_s, y_s) P(x_s, y_s) \tag{3.1.12}$$

The field after the aperture contains the field before the aperture, $U_s^-(x_s, y_s)$ multiplied by the aperture function, $P(x_s, y_s)$. Fourier methods employed on the Fraunhofer diffraction integral becomes:

$$U_o(\boldsymbol{r}_o) = -\frac{iexp(ikz_o)}{\lambda z_o} \exp\left[\frac{ik}{2z_o}(x_o^2 + y_o^2)\right] \boldsymbol{F}_\xi \boldsymbol{F}_\eta \{U_s^+(x_s, y_s)\} \tag{3.1.13}$$

The image quality for segmented primary mirror telescopes can be determined by the quality of the point spread function (PSF) [15]. When the object is far like a star the incoming wavefront the aperture can be considered to be a plane wave. Thus, for coherent imaging the impulse response field or PSF to a telescope system can be written as the Fourier transform of the aperture function:

$$\text{PSF} = \boldsymbol{F}_{\xi}\boldsymbol{F}_{\eta}\{P(x_s, y_s)\} \tag{3.1.14}$$

Table 1 provides a summary of the equations derived above [12].

| PSF | Equation (convolutional form) | When used | Wavefront |
|---|---|---|---|
| Huygens | $\frac{\left(-\frac{i}{\lambda}+\frac{1}{2\pi r_{o_s}}\right)\gamma_z \exp\left(ikr_{o_s}+\emptyset\right)}{r_{o_s}}$ | Valid for all values of $z_o$ | Spherical |
| Fresnel | $-\frac{iexp(ikz_0)}{\lambda z_0}\exp\left(\frac{ik}{2z_o}[(x_o-x_s)^2+(y_o-y_s)^2]\right)$ | When $z_o \gg \sqrt[3]{\frac{\pi}{4}}\,\lambda\left(\frac{\frac{D_{ap}}{2}}{\lambda}\right)^{4/3}$ | Parabolic |
| Fraunhofer | $-\frac{iexp(ikz_0)}{\lambda z_0}\exp\left(\frac{-ik}{z_o}[x_o x_s + y_o y_s]\right)$ | When $z_o \gg \frac{\pi}{\lambda}\left(\frac{D_{ap}}{2}\right)^2$ | Planar |

**Table 1. PSF summary.**

### 3.2. Software Package: HCIPy

High Contrast Imaging for Python (HCIPy) is an open-source software package for simulating physical optics propagation, developed by teams of astronomers at Leiden University [7]. The software package is open to modifications from software developers and scientists around the world. It propagates the complex electro-magnetic wavefront through the defined optical system using Fresnel or Fraunhofer diffraction integrals from scalar diffraction theory [7]. HCIPy is written in the Python language, a high-level programming language that is in use by many astronomical projects. HCIPy is commonly used for high-contrast imaging simulations including wavefront analysis and coronagraphic systems [16]. This

package minimizes user errors by the use of classes, which the user rarely interacts with directly. This architecture controls much of the mathematical details and sampling requirements in the background. Instead, the user interacts with functions mostly to focus strictly on the system details rather than the details [16]. The components in HCIPy are written independently allowing for a modular architecture of the optical elements involved.

HCIPy allows for custom optical elements to be created and propagate the wavefront. Alternatively, the user can implement pre-created aperture functions for the same use. A **Grid** class is used to determine sampling of an N-dimensional space, which consists of the **Coords** class, which provides the coordinate positions in either polar or cartesian for a telescope pupil to reside. The function **make_pupil_grid()** implements the **Grid** and **Coords** classes to create a regularly spaced cartesian grid that is symmetric about the origin. A **Field** object is considered a discretized version of a physical field, such as temperature, potential, electric field, or intensity. The **Field** contains a **Grid** and an array of values. A **Field** can be operated on by a Fast Fourier Transform (FFT), which is a discretized Fourier Transform algorithm, to return another **Field** that has a **Grid** with corresponding frequency units. HCIPy is responsible for keeping track of the sampling in the background throughout the code, which makes it difficult to introduce human errors to sampling. The function **make_focal_grid()** creates a separate cartesian grid and takes parameters that allow control of the number of pixels per diffraction of the PSF.

The Hexagon Segmented Mirror uses a **Field** generator, which is a mathematical description of some geometry, to create the telescope pupil in the shape of hexagonal segments. Another function is use to allow each of the segments individually deformed using Piston, Tip, and Tilt as its inputs. The parameters can be modified to create the geometry needed. A **Wavefront** object is then created to represent the incoming waves Electric field. The **Wavefront** is passed from the telescope pupil grid to the focal grid by using the **Propagator** function via FFT using either Fresnel or Fraunhofer approximations.

The Pinwheel Segmented Mirror is constructed in a more manual way. Each segment is built in a polar coordinate system individually. The segments are then manually placed into the telescope pupil grid

at their precise location. A separate **SurfaceApodizer** is used to simulate misalignment of each of the segments. Each Apodizer is only disturbed over the segment being called. All the Apodizers are then added together, which creates a 2-dimensional custom Apodizer. The incoming wavefront is then retarded or advanced in phase depending on the segment's misalignment. The same propagator function used above is then used to pass the wavefront from the pupil to the focal grid.

Verification was done to ensure these two models were equivalent. The center segment of each telescope pupil was isolated while all other segments were set to zero. The segment was given exactly 1 wave of tilt. The axis of tilt is exactly the center of the segment. The angle of tilt was set to $\pi$ radians so that the edge tilting toward the focal plane was $+\pi$ radians and the edge tilting away from the focal plane was $-\pi$ radians. Each angle represents, $\frac{\lambda}{2}$ nano-meters of tilt. The total tilt in nano-meters, adding both sides, is therefore 1 wave. The full aperture diameter is set to, $D$ for each telescope. Each telescope has 5 segments that span $D$. The distance to the focal plane is the focal length, $F$. Using similar triangles:

$$PSF_{shift} = \frac{2\lambda}{D_{segment}} * F \tag{3.2.1}$$

The factor of 2 comes from Snell's law for reflection, and the focal length is 90 meters. The diameter of the segment is a fifth of the full telescope diameter, therefore the PSF shift for 1 wave of tilt is $10\frac{\lambda}{D}$. This was done for each telescope pupil, Hexagon and Pinwheel. See Figure 1 below.

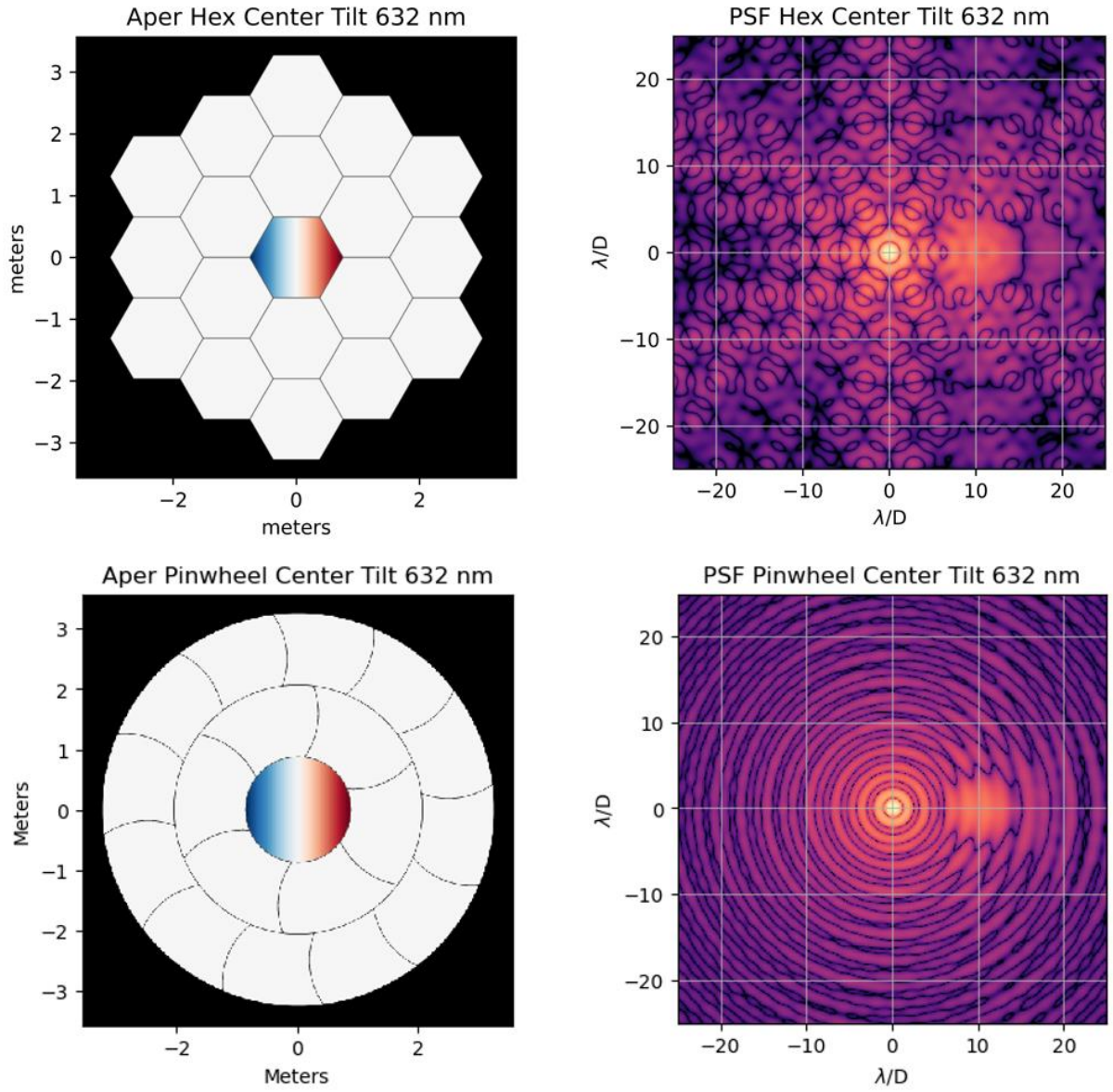


**Figure 1. HCIPy verification of simulation. Display of HCIPy code implementation for verification of equitable comparison. It is expected with the input of 1 wave of Tilt the PSF would shift 10 units of $\lambda/D$.**

# 4. SEGMENTATION TOPOLOGY

## 4.1. Hexagonal Segmentation

The Hexagonal Segmented Mirror is comprised of 18 segments with the center segment not included. The geometry of the mirror is comparable to the JWST. The full diameter of the aperture in the y-axis is 6.5 meters. The full diameter of the aperture in the x-axis is ~ 6.004 meters. A single segment flat to flat is defined as the full diameter divided by 5. The length of one side of a single segment is ~0.751 meters. The area of a single segment is calculated to be 1.95 meters-squared. The center obscuration is exactly the shape of single segment. The aperture is arranged from the center gap outward in a honeycomb pattern. The total area of the Hexagonal Segmented Mirror is 34.92 meters-squared. Every gap between each segment is 10 mm. See Figure 2 displaying the Hexagonal Segmented Mirror.

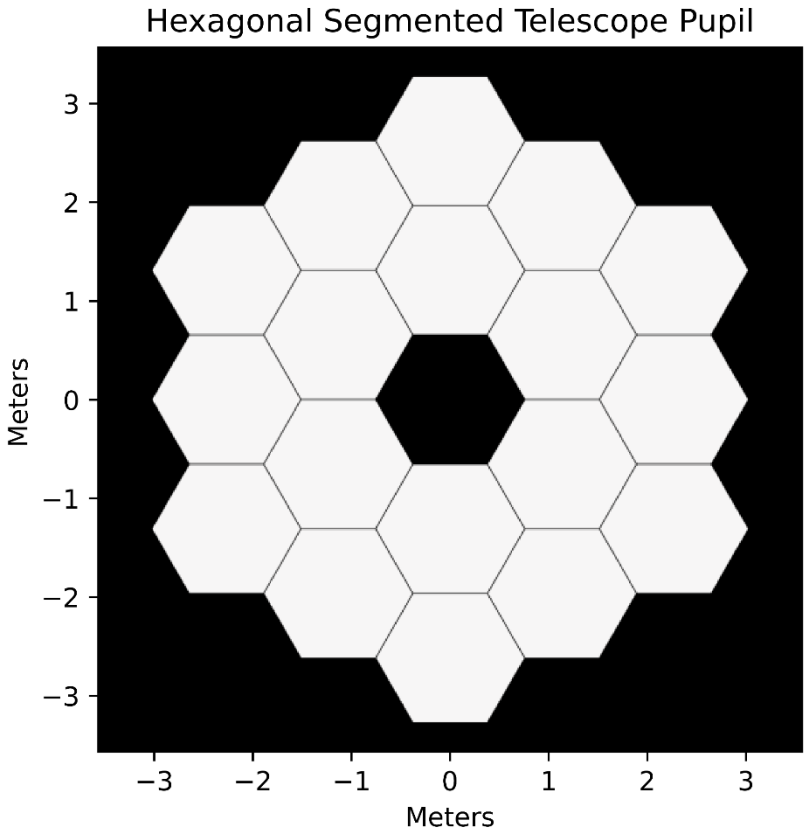


**Figure 2. Display of the Hexagonal Segmented Mirror Telescope Pupil.**

### 4.2. Pinwheel Segmentation

The Pinwheel Aperture builds upon the theory of implementing a curved secondary spider to fanout the diffraction spikes caused by the straight edge obscurations in the pupil, and the modeling of the 10-meter Pinwheel Pupil, which uses circular shaped spokes to form the edges of each segment that stretch the radius of the aperture and are azimuthally divided [10, 11]. If the number of spokes across the aperture add to an integer multiple of semicircles, the PSF will achieve the desired effect [7]. To explain the Topology for the Pinwheel construction the derivation from Derby for an 18-segment pupil will be referenced, however the Pupil used in this report was modified to have nearly equal segments to be directly comparable with the hexagonal segments [7]. The diameter of Pinwheel aperture is 6.5 meters. There are 18 total segments not including the center circular segment gap. The circular segment gap is 0.8725 meters in diameter. The center circular obscuration is located at x=0, y=0. Converting to a polar grid will be useful for describing the segment's relative locations, where all radius' will be with respect to the center circular gap. The Pinwheel aperture can be divided into 2 rings not including the central circular gap that the segments lie on. The first ring is the inner ring that is closest to the central circular gap and the second ring is the outer most ring. The first ring of segments inner radius is 0.8825 meters. The first ring of segments outer radius is 2.05875 meters. The second ring of segments inner radius is 2.06875 meters. The second ring of segments outer radius is 3.245 meters. The gaps between the segments are 10 mm. The inner ring of segments has 6 spokes. The inner ring radius of the spokes are solved for in Derby's paper by,

$$R = \frac{(r_{ap} - r_c)}{2\sin\left(\frac{\pi n}{2N_{spoke}}\right)}$$

which equates to 2.3725 meters [7]. Where $r_{ap}$, is the radius of the aperture, $r_c$, is the radius of the central circular gap plus the gap size, $n$, is the integer number of semi-circles the spokes make, and $N_{spoke}$, is the number of spokes. The outer ring of segments has 12 spokes. The outer ring spokes radius are equal to the

inner ring spokes radius. The inner ring of segments each have a surface area of 1.86212 meters-squared. The outer ring of segments each have a surface area of 1.63988 meters-squared. The total area of the Pinwheel telescope pupil is 30.8512 meters-squared. See Figure 3 displaying the Pinwheel Segmented Mirror.

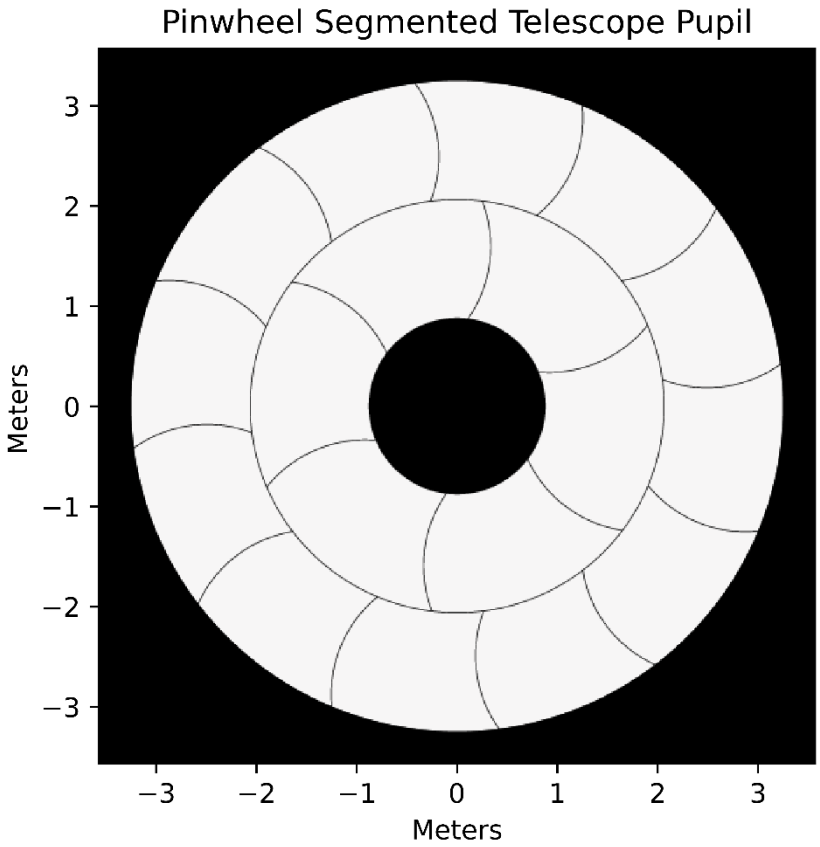


**Figure 3. Display of the Pinwheel Segmented Mirror Telescope Pupil.**

## 5. NOMINAL PSF SIMULATION RESULTS

Both apertures, Hexagonal and Pinwheel, were input with the same system parameters. The wavelength used was 632.8e-9 meters. The focal length, propagation distance from pupil grid to the focal grid is 90 meters. The pixels per image are 512 x 512. The sample rate used is 20, well over the diffraction limited sampling rate. Increasing the pixels slowed down the software so high-resolution

images were not readily available, so instead the sampling rate was increased and sample spacing decreased. The airy rings being shown for both PSFs are 20. The units for the PSFs are in angular space, $\lambda/D$.

### 5.1. Hexagonal PSF

The Hexagonal Aperture PSF bears many features. The central energy spot is attained by the smooth inscribed circles, and rectangular shapes creating low order frequencies. The central spot diameter is associated with the inscribed circle created by the inner edges of the entire aperture. The second dark circle diameter in the PSF is associated with the inner inscribed circle diameter of the central segment. The sharp edges and corners create higher-order frequencies that contribute to the flare effects. Within the aperture there are repeating periodic hexagonal shapes of different diameters and spatial locations, which create ordered harmonics that contribute to the periodic features seen throughout the PSF. Figure 4

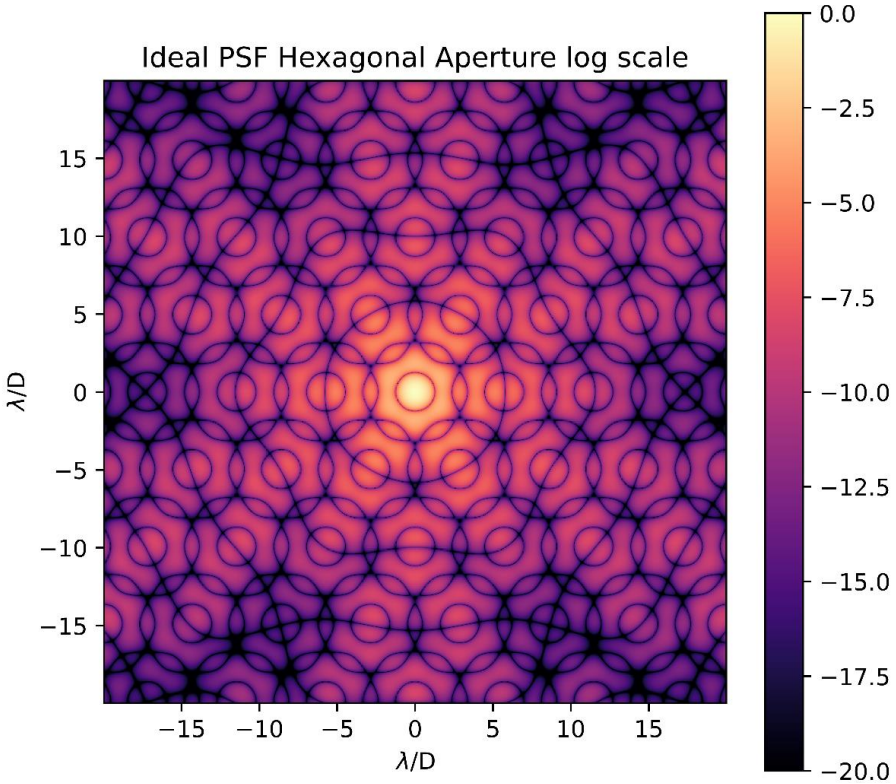


displays the PSF for the Hexagonal Segmented Mirror with absolutely 0 misalignment error.

**Figure 4. Display of the Hexagonal Segmented Telescope Pupil Ideal PSF Intensity in log scale.**

Section 2.5 above alluded to what is being seen from the hexagonal PSF here. Each pair of parallel edges from the segments creates a grating like structure on the pupil. The resulting PSF carries perpendicular

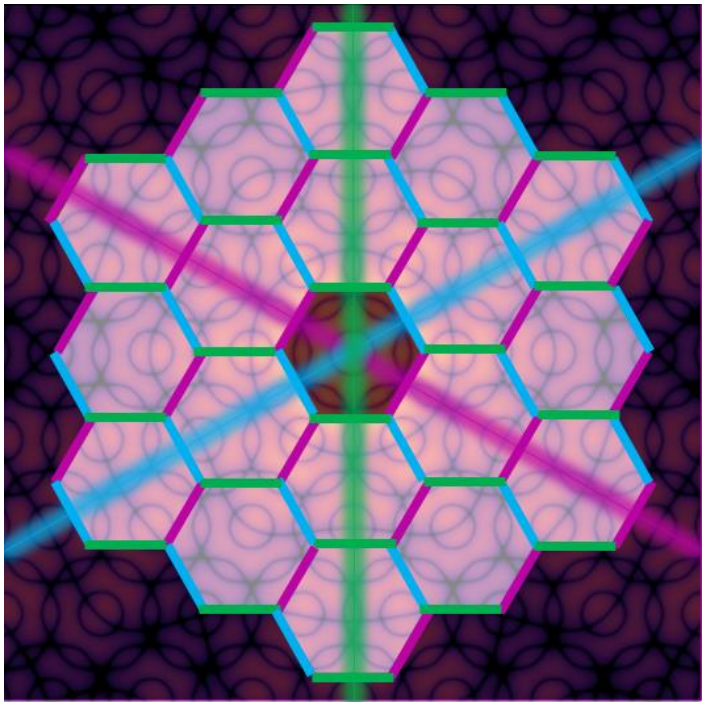

flares or spikes to the edges of the segment in the pupil [7]. Figure 5 displays the PSF overlaid on the pupil to illustrate the diffraction spikes emanating from the center of the PSF [7].

**Figure 5. Display of the Hexagonal Segmented Telescope Pupil overlaid by the Ideal PSF. The edges of the segments have been color coated to further illustrate the diffraction grid on the pupil, which results in diffraction flares perpendicular to those edges.**

The center spot and the diffraction flares are repeated throughout the focal grid, although much darker. This can be explained as the diffraction from the other edges out-side the center segment interfering with each other at the focal plane. These effects are not viewable without the log scale.

### 5.2. Pinwheel PSF

Figure 6 displays the PSF for the Pinwheel Segmented Mirror with absolutely 0 misalignment error. The Pinwheel PSF color scale is the same as the Hexagonal PSF color scale for a direct comparison.

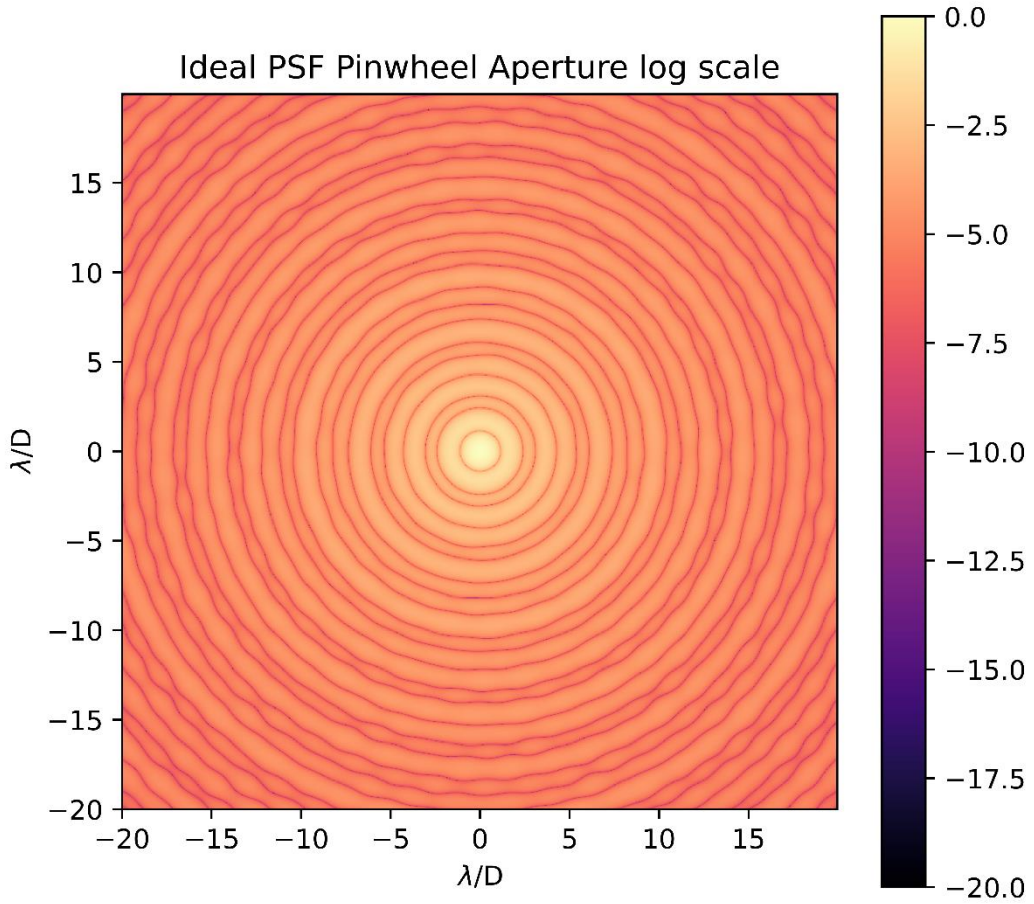


**Figure 6. Display of the Pinwheel Segmented Telescope Pupil Ideal PSF in log scale.**

The curved spokes in the Pinwheel pupil are intended to fan out diffraction effects from the grating like obstructions created by the edges of the segments. As seen in Figure 6 the energy is evenly distributed so these flares or spikes are no longer apparent, creating a less dense energy concentration at the center compared to the hexagonal case. The circular edges can be considered as an infinite amount of tiny rectangular functions oriented along a spherical curve. The resulting PSF resembles a bow-tie, which is the cause of the energy fan-out. The arc length of the bow-tie corresponds to the arc length of the

circular edge. The energy distributed from the flares brighten the higher order rings in the PSF. The airy rings, or the zeros in the Intensity distribution of the PSF are not evenly spaced. This is caused by the diameter differences from the center circular gap and the Pinwheel Aperture full diameter. The rings width is smaller than the center gap creating a difference in zero values once the FFT is taken. A wide diameter in the pupil plane results in a narrower airy ring in the focal plane, which is the center gap. A small diameter in the pupil plane results in a wider airy ring in the focal plane. In other words, the subtraction of these two diameters results in a subtraction of the two corresponding Bessel functions in Fourier space creating rings that are not evenly spaced.

# 6. PSF SENSITIVITY RESULTS

## 6.1. Hexagonal Segment Random Piston Study

Piston is defined here as a misalignment distance where the segment plane is translated either in front of the aperture plane or behind the aperture plane. This section will display 12 piston values that gradually increase. The Piston value will be applied randomly for each segment as + (plus) or – (minus) the value given. For this study the airy rings shown is set to 20. The Piston values given are 0nm, 10 nm, 20 nm, 30 nm, 40 nm, 50 nm, 60 nm, 70 nm, 80 nm, 90 nm, 100 nm, and 1 mm. Figure 7 displays the Piston misalignment on the Hexagonal Aperture. Figure 8 displays the corresponding PSFs.

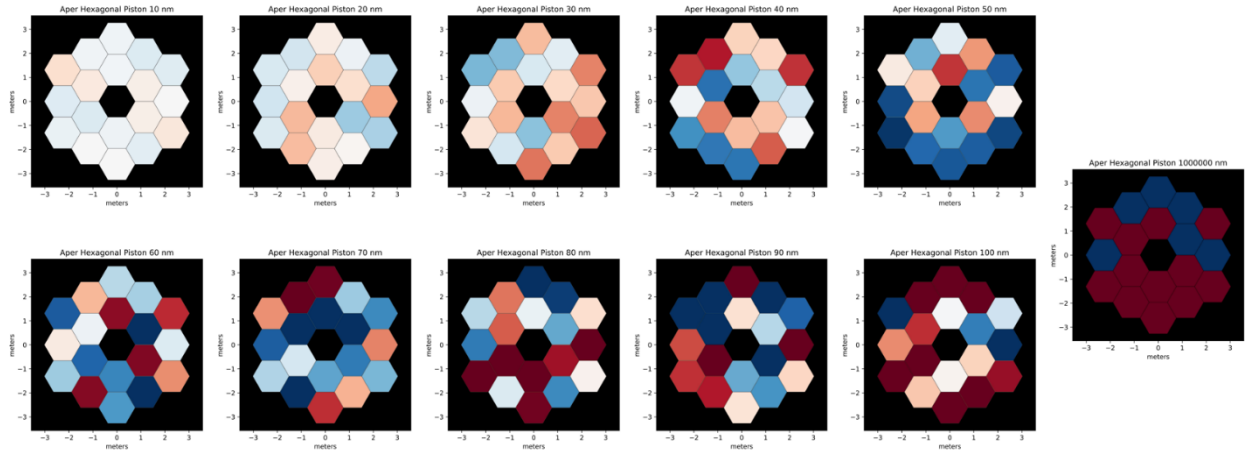


**Figure 7. Display of the Hexagonal Segmented Telescope Pupil with the random Piston values on each of the segments. The color scale is set to the 100 nm value to show the Piston amount increase.**

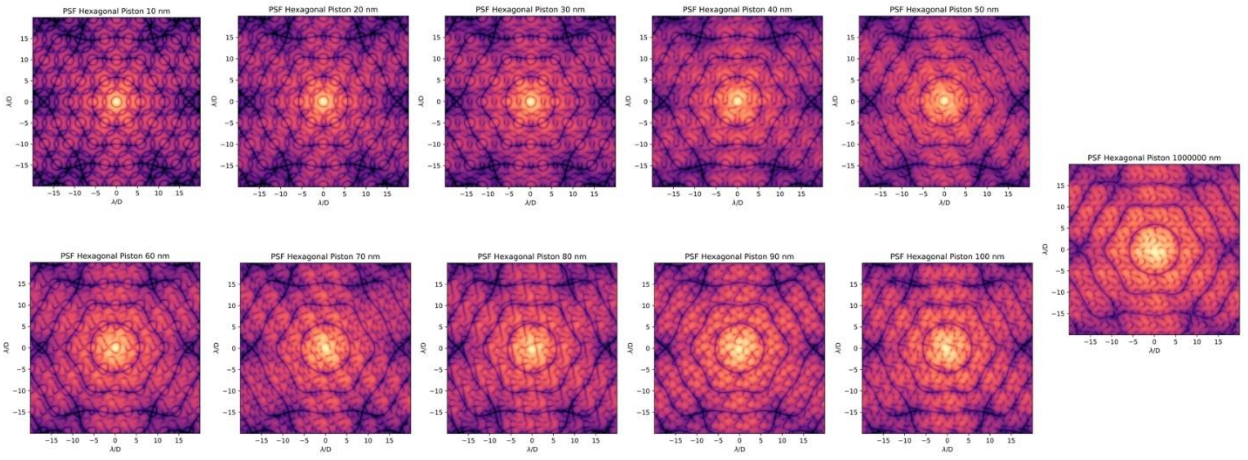


**Figure 8. Display of the corresponding PSFs for the Hexagonal Segmented Telescope Pupil with the random Piston values on each of the segments.**

As the piston values increase the energy in the center spot begins to increase, as seen in Figure 8. This can further be seen in Figure 9. The encircled energy radius (EER) is defined as the circle of radius equal to the point where 90% of the energy for the center spot is contained within. The Hexagonal Segmented Aperture Ideal PSF EER begins at 0.742 $\lambda/D$. The airy radius is defined as 1.22 $\lambda/D$, where

the first 0 is located, which is 100% of the center spot radius. The PSF from 100 nm of Piston misalignment expands the EER to 2.52 $\lambda/D$, which is 3.4 times the ideal PSF EER. Eventually the Piston misalignment will expand the EER to number of segments across the aperture, which is 5 times the ideal PSF EER. The piston introduces no shift to each segmented PSF, which are stacked concentrically in the image plane. There are 18 segments that contribute the same geometry, creating 18 identical PSF copies, however out of phase. Therefore, the rings remain in the PSF at large piston values, while the periodic features become washed out. The limit becomes for center spot expansion becomes 3.71 $\lambda/D$. The Piston value for 1 mm reaches 3.34 $\lambda/D$, which is 4.5 times the ideal PSF EER.

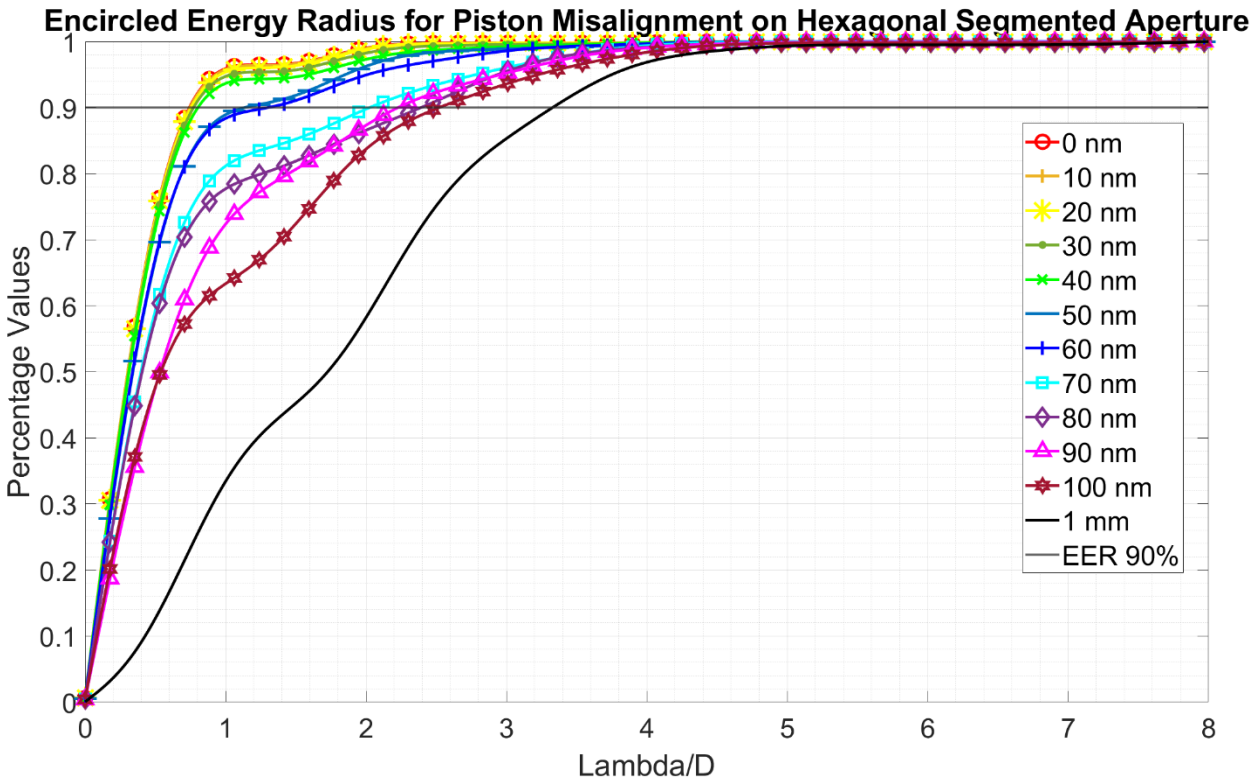


**Figure 9. Display of the EER corresponding to PSFs for the Hexagonal Segmented Telescope Pupil with the random Piston values on each of the segments.**

### 6.2. Pinwheel Segment Random Piston Study

The Piston values used for the hexagonal case are the same used for the Pinwheel case. The Pinwheel Segmented Aperture Ideal PSF EER begins at 0.698 $\lambda/D$. The PSF from 100 nm of Piston misalignment expands the EER to 1.99 $\lambda/D$, which is 2.85 times the ideal PSF EER. Eventually the Piston misalignment will expand the EER to 5 times the ideal PSF EER, which is 3.49 $\lambda/D$. When compared to the Piston case for the Hexagonal Aperture the rings of the PSF are quickly washed out. This is explained by the fact that each segment is oriented and geometrically different. When piston is applied each segment contributes a unique PSF, which are out of phase, and therefore was out the outer rings. The Piston value for 1 mm reaches 2.88 $\lambda/D$, which is 4.12 times the ideal PSF EER. Figures 10, 11 and 12 display the Pinwheel aperture with the random Piston values on each segment, the corresponding PSFs, and the EER plot, respectively.

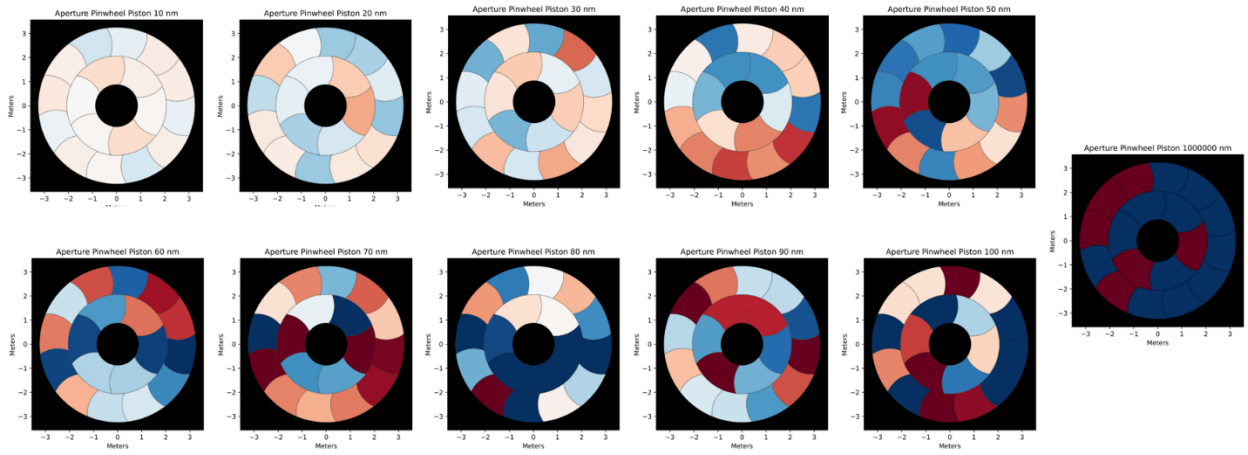


**Figure 10. Display of the Pinwheel Segmented Telescope Pupil with the random Piston values on each of the segments. The color scale is set to the 100 nm value to show the Piston amount increase.**

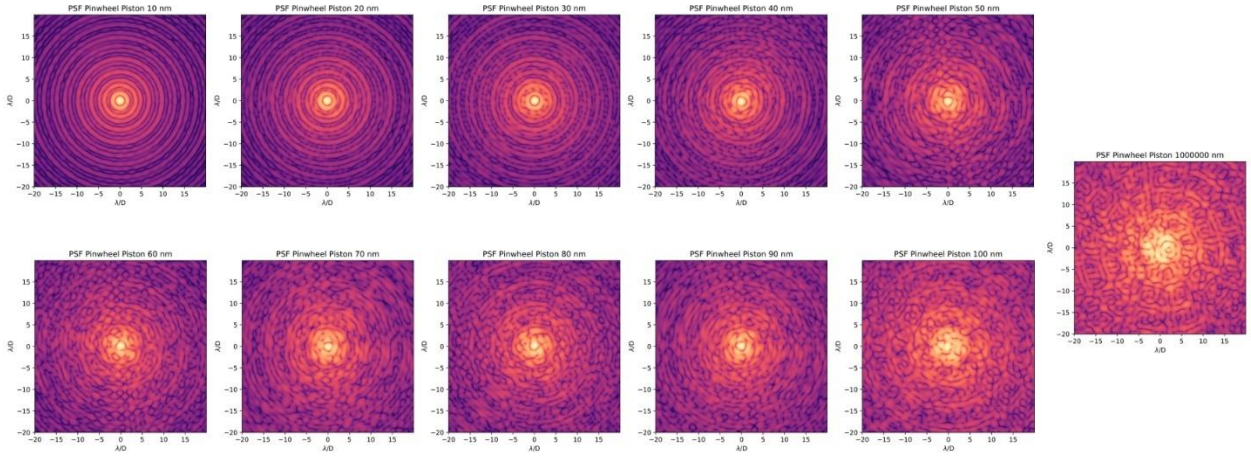


**Figure 11. Display of the PSFs for Pinwheel Segmented Telescope Pupil with the random Piston values on each of the segments.**

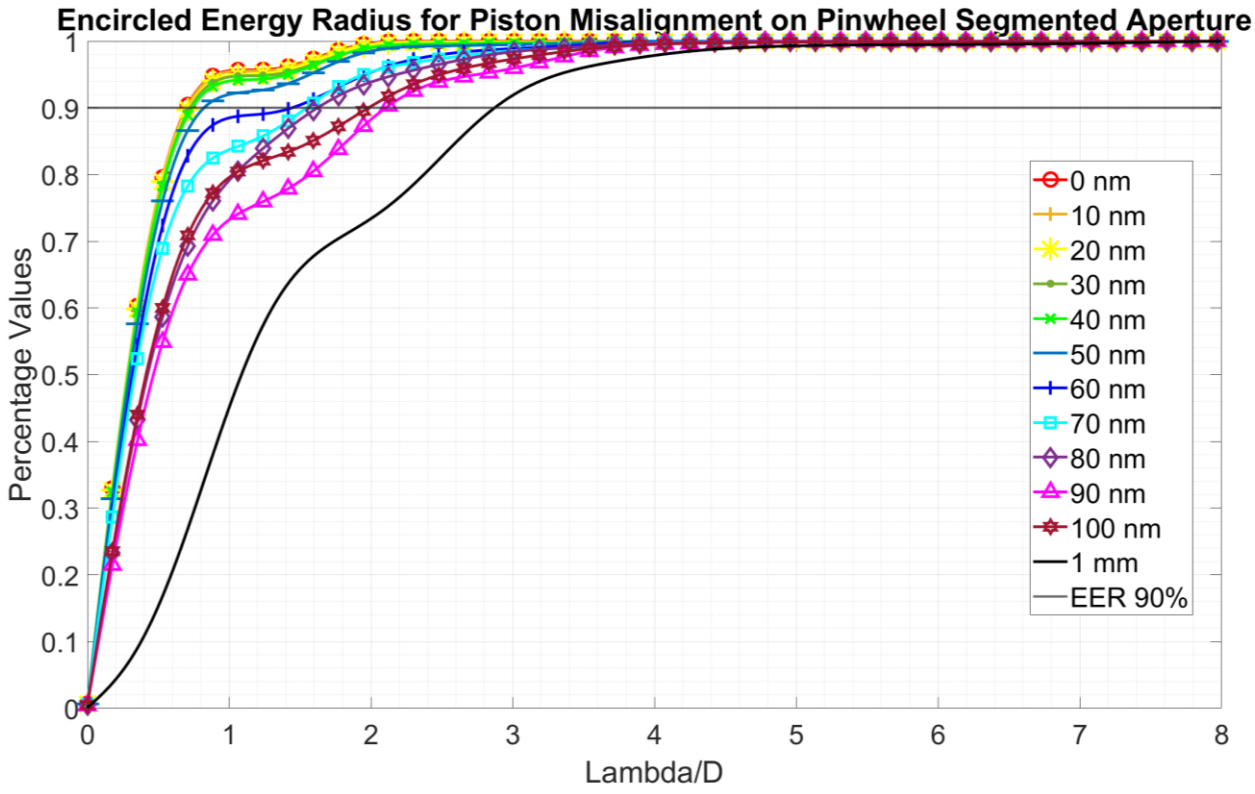


**Figure 12. Display of the EER corresponding to PSFs for the Pinwheel Segmented Telescope Pupil with the random Piston values on each of the segments.**

### 6.3. Hexagonal Segment Random Tip/Tilt Study

Tip/Tilt is defined here as a misalignment rotated around the center point of each segment. The segmented is tilted in radians where the $\tan(\emptyset) = \frac{[Tip\ Tilt\ value\ in\ nm]}{\left[\frac{diam_{segment}}{2}\right]}$. The tilted segment is then randomly azimuthally rotated around the center point. The angle of tilt is related to the wavelength by $\emptyset = 2\pi * \frac{[Tip\ Tilt\ value\ in\ nm]}{\lambda}$. This section will display 12 Tip/Tilt values that gradually increase. The Tip/Tilt value will be applied randomly for each segment as + (plus) or – (minus) the value given. The Tip/Tilt values given are 0 nm, 25 nm, 50 nm, 75 nm, 100 nm, 125 nm, 150 nm, 175 nm, 200 nm, 225 nm, 250 nm, and 10 waves (~3191 nm). The values correspond the following input angles in nano-radians are calculated in Table A-5 in the Appendix. Figure 13 displays the Tip/Tilt misalignment on the Hexagonal Aperture. Figure 14 displays the corresponding PSFs. Figure 15 displays the EER for the Tip/Tilt Hexagonal case. The EER continuously degrades as more tilt is introduced. The tilt of each segment shifts each segment PSF to different locations resulting in 18 PSF, that do not overlap in the image plane. At 10 waves of Tip/Tilt the EER expands to 7.42 $\lambda/D$, which is 10 times the Ideal EER.

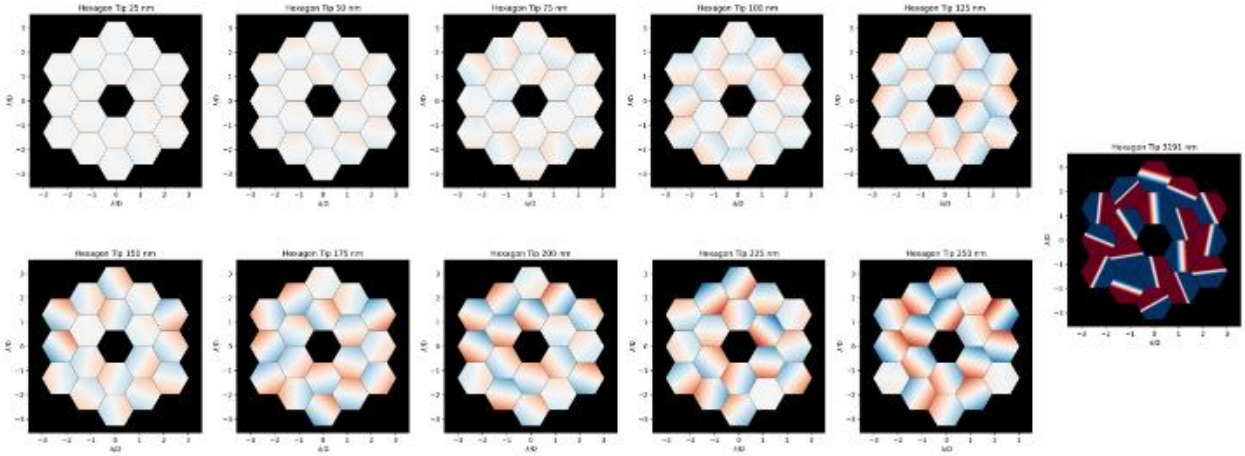

**Figure 13. Display of the Hexagonal Segmented Telescope Pupil with the random Tip/Tilt values on each of the segments. The color scale is set to the 250 nm value to show the Tip/Tilt amount increase.**

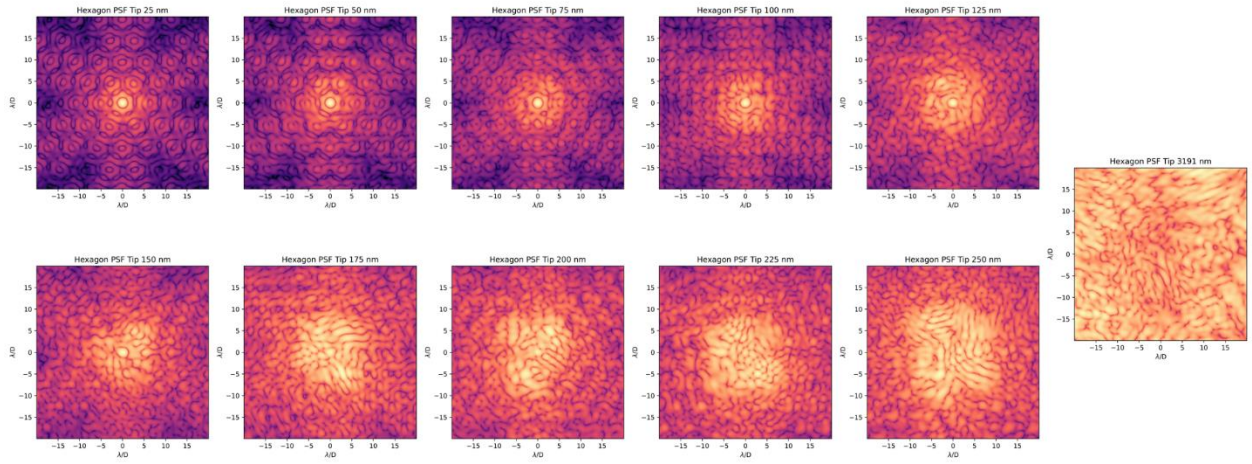


**Figure 14. Display of the PSFs for the Hexagonal Segmented Telescope Pupil with the random Tip/Tilt values on each of the segments.**

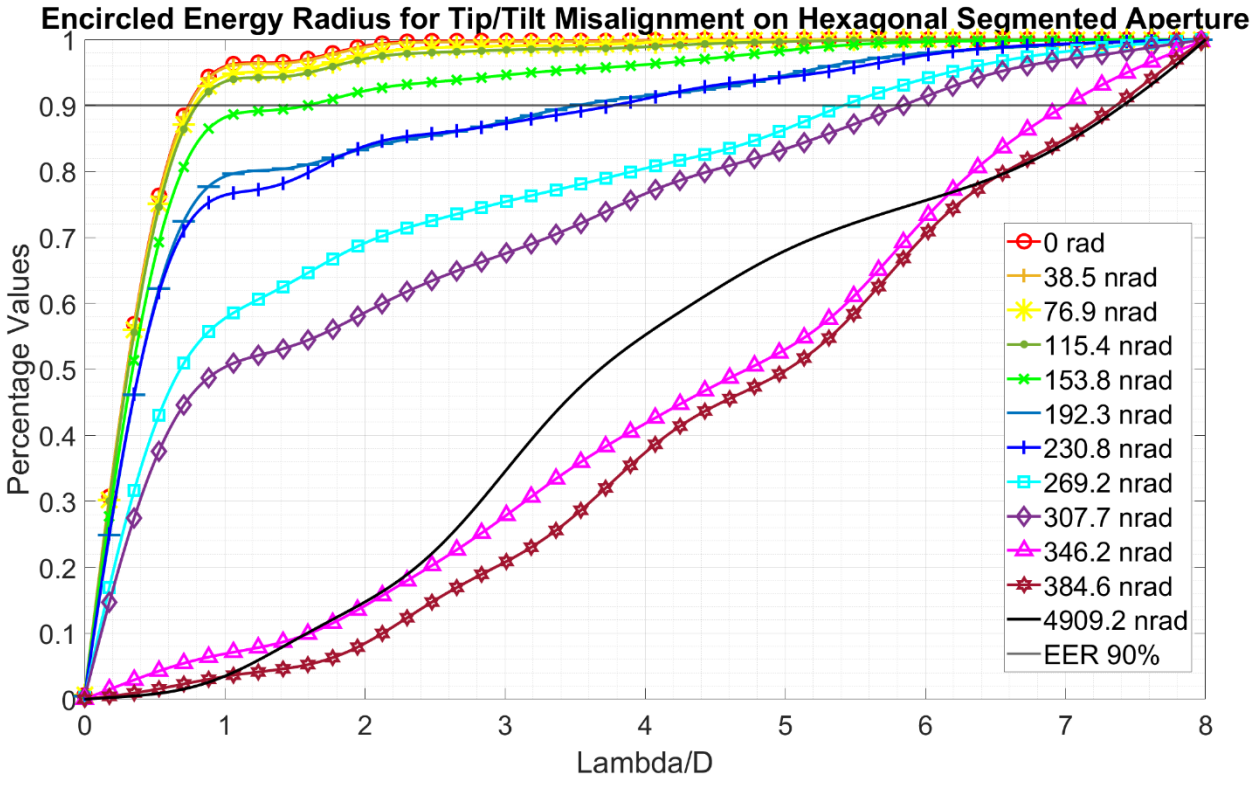


**Figure 15. Display of the EER corresponding to PSFs for the Hexagonal Segmented Telescope Pupil with the random Tip/Tilt values on each of the segments.**

### 6.4. Pinwheel Segment Random Tip/Tilt Study

The Tip/Tilt values used for the Hexagonal case is the same used for the Pinwheel case. Figures 16, 17 and 18 display the Pinwheel aperture with the random Tip/Tilt values on each segment, the corresponding PSFs, and the EER plot, respectively. At 10 waves of Tip/Tilt the EER expands to 7.22 $\lambda/D$, which is 10.34 times the Ideal EER.

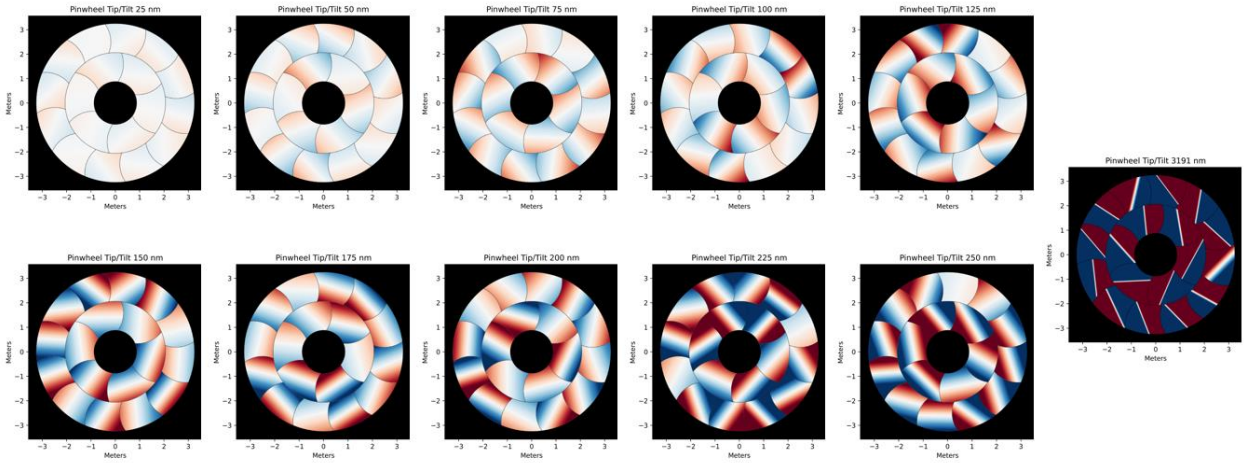


**Figure 16. Display of the Pinwheel Segmented Telescope Pupil with the random Tip/Tilt values on each of the segments. The color scale is set to the 250 nm value to show the Tip/Tilt amount increase.**

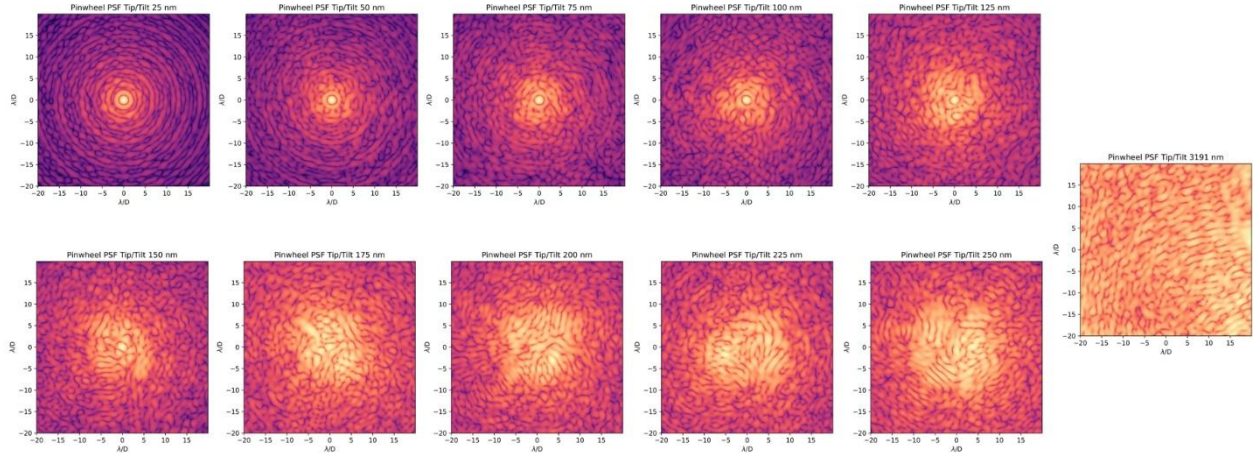


**Figure 17. Display of the PSFs for the Pinwheel Segmented Telescope Pupil with the random Tip/Tilt values on each of the segments.**

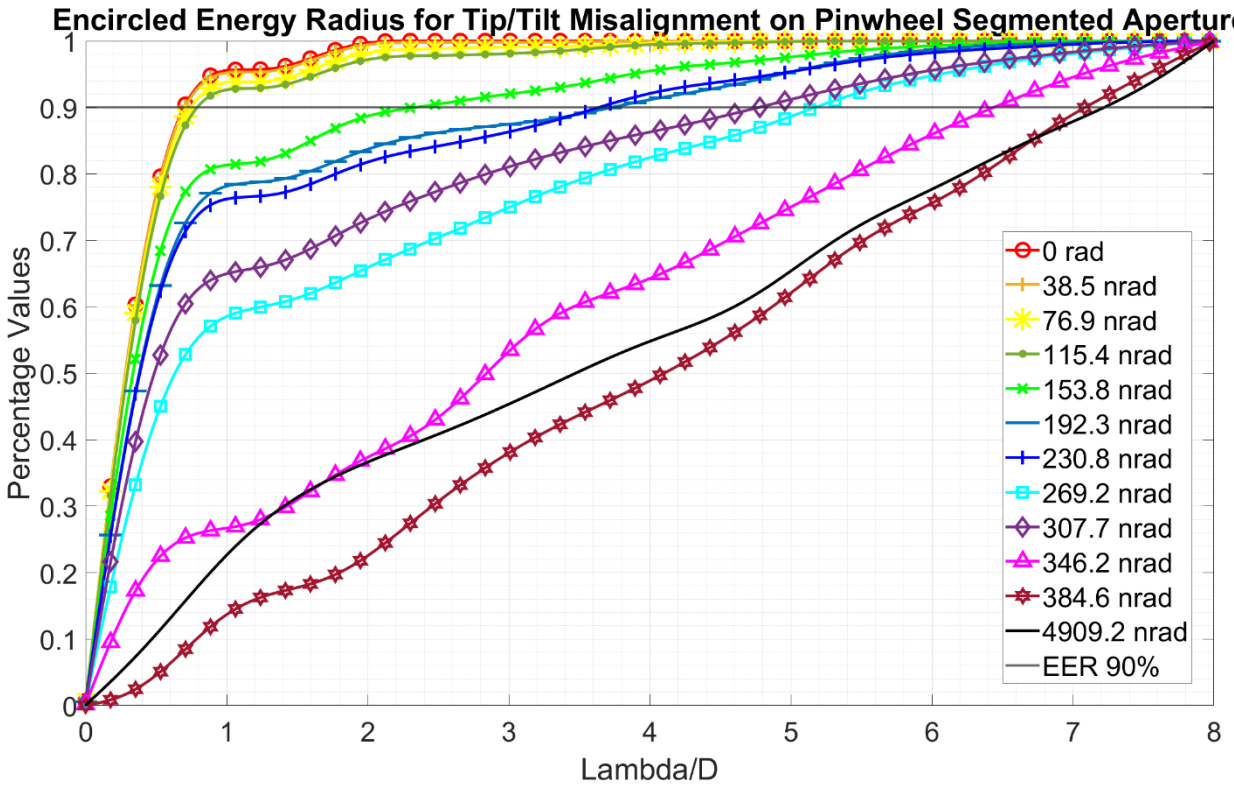


**Figure 18. Display of the EER corresponding to PSFs for the Pinwheel Segmented Telescope Pupil with the random Tip/Tilt values on each of the segments.**

### 6.5. Summary of EER Study

Table 2 and 3 below contain the summary for each EER case study and a comparison using the starting Ideal case with 0 misalignment. The expansion of the 90% point in $\lambda/D$ is divided by the Ideal case to produce a value for how many Ideal cases each misalignment expanded the central energy spot. Table 2 and 3 serve two purposes: a verification that the Misalignments are producing the results that are theoretically expected, and a comparison of for how the central energy spot is expanded for both Aperture types relative to their starting positions. Due to the random nature of the study the values do not expand the center spot energy in a linear fashion. However, the table clearly shows that the misalignments degrade the PSFs in the way one would expect. The Piston Misalignment reaches a peak near 5X the

Ideal, which is caused by the 5 segments that span the Full Aperture Diameter. The Tip/Tilt Misalignment does not reach a peak as expected, but degrades the PSFs as more angle is introduced.

| Table 1. PISTON MISALIGNMENT | | | | |
|---|---|---|---|---|
| [nm] | Hexagonal [λ/D] | X Ideal | Pinwheel [λ/D] | X Ideal |
| 0 | 0.7423 | | 0.6979 | |
| 10 | 0.7457 | **1.0047** | 0.7005 | **1.0038** |
| 20 | 0.7555 | **1.0178** | 0.7154 | **1.0251** |
| 30 | 0.7719 | **1.0399** | 0.7249 | **1.0388** |
| 40 | 0.8031 | **1.0819** | 0.7391 | **1.0591** |
| 50 | 1.1343 | **1.5282** | 0.8227 | **1.1789** |
| 60 | 1.2998 | **1.7511** | 1.4425 | **2.0670** |
| 70 | 2.0249 | **2.7280** | 1.5457 | **2.2150** |
| 80 | 2.3913 | **3.2216** | 1.6227 | **2.3252** |
| 90 | 2.2279 | **3.0014** | 2.1042 | **3.0152** |
| 100 | 2.5197 | **3.3946** | 1.9828 | **2.8412** |
| 1 [mm] | 3.3284 | **4.4841** | 2.8726 | **4.1163** |

**Table 2. Documentation of the EER study for the Piston Misalignment of each Segmented Aperture.**

| Table 2. TIP/TILT MISALIGNMENT | | | | |
|---|---|---|---|---|
| [nrads] | Hexagonal [λ/D] | X Ideal | Pinwheel [λ/D] | X Ideal |
| 0 | 0.7423 | | 0.6979 | |
| 38.5 | 0.7471 | **1.0065** | 0.7045 | **1.0095** |
| 76.9 | 0.7781 | **1.0483** | 0.7461 | **1.0692** |
| 115.4 | 0.8009 | **1.0790** | 0.7911 | **1.1337** |
| 153.8 | 1.5863 | **2.1370** | 2.3355 | **3.3466** |
| 192.3 | 3.5169 | **4.7380** | 3.7313 | **5.3467** |
| 230.8 | 3.7732 | **5.0833** | 3.6385 | **5.2137** |
| 269.2 | 5.4161 | **7.2967** | 5.1728 | **7.4123** |
| 307.7 | 5.8382 | **7.8653** | 4.7725 | **6.8387** |
| 346.2 | 6.9986 | **9.4285** | 6.4376 | **9.2247** |
| 384.6 | 7.3612 | **9.9171** | 7.0870 | **10.1552** |
| 4909.2 | 7.4111 | **9.9844** | 7.2220 | **10.3487** |

**Table 3. Documentation of the EER study for the Tip/Tilt Misalignment of each Segmented Aperture.**

# 7. PSF PERFORMANCE BASED ON MONTE CARLO SIMULATION

For the Monte Carlo Simulation each Aperture, Hexagonal and Pinwheel, segments were introduced the same amount of random misalignment per segment. The case studies for Piston and Tip/Tilt were done separately with the goal of identifying which Telescope Pupil may be less sensitive to inevitable misalignment by the support structures. The experiment was run 10 times for each case, for each Aperture in order to calculate an average and a standard deviation. The measure of quality common to each study was the average EER for each PSF and the average Strehl Ratio for each PSF. The Strehl Ratio is here is defined as the Ideal Segmented PSF center pixel value divided by the Misaligned Segmented PSF center pixel value. The random misalignment values were input into HCIPy and the corresponding non log PSFs were exported saving the pixel data. The images were then imported into Matlab, where a series of manually typed scripts processed the image to arrange each pixel value to range from 0 to 255, 0 being black and 255 representing white. The scripts used a common center pixel corresponding to the half-way point in x and y for each image. The scripts began at the center pixel, representing (0,0) in (x,y) cartesian space. A grab arm function was created to sweep through pixel values and store them into a separate vector adding each series of values as they swept the image. The arm's 1$^{st}$ position was pixel (1,0). The arm would grab this value and then rotate about the center point, $2\pi$ radians grabbing every pixel it would touch minus the final pixel value, and adding these values along the way, creating a ring (perimeter) of brightness values. This value was stored in the separate vector as the first position. Then the arm would extend to (2,0) and sweep again. This process repeated until the edge of the image. The vector was fully populated with every arm grabber length, representing the total image brightness contained within the arm grabber's ring (perimeter). An Integral function was created to integrate the vector of brightness rings to create vector_2, representing the brightness contained within each circle (area). Vector_2 was then normalized by the entire summed image brightness, the last column of vector_2. This was then plotted as a function of the proper $\lambda/D$. An interpolation function was created to sift vector_2 to extract the 90% EER point for each image. A schematic diagram depicting the flow of data and image processing

described above is displayed below in Figure 19. A second function was created to extra each image's center pixel value. Table A-1, A-2 in Appendix contains the extracted data from the scripts above for each image associated with the Piston Misalignment routine. Table A-3, A-4 in Appendix contains the extracted data for each image associated with the Tip/Tilt Misalignment routine. Figure 20 and 21 contains the Piston misalignment comparison study for Hexagonal Segmented Mirror vs Pinwheel Segmented Mirror for the EER and Strehl Ratio of each mirror type, respectively. Figure 22 and 23 contains the Tip/Tilt misalignment comparison study for the EER and Strehl Ratio of each mirror type.

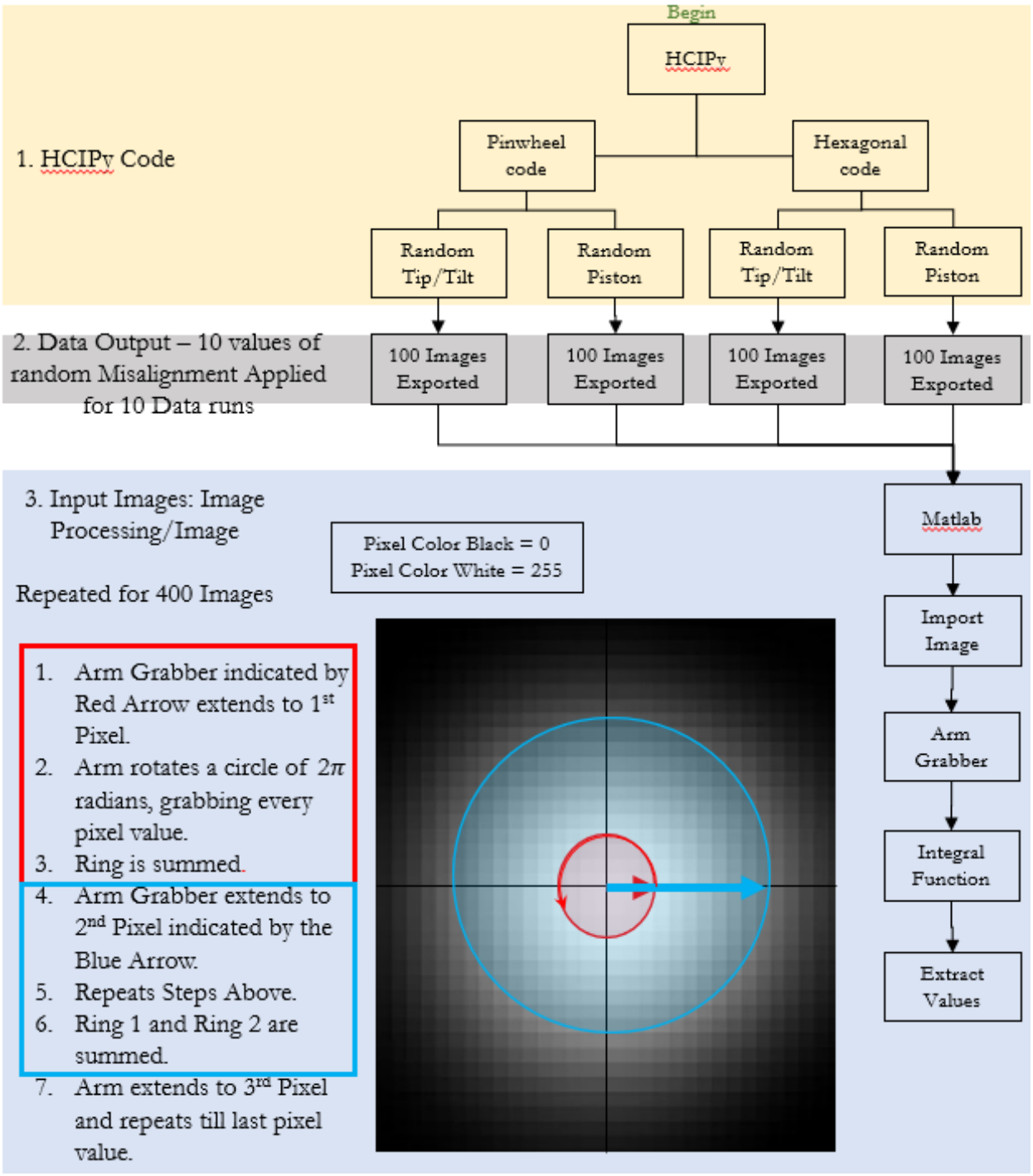


**Figure 19. Schematic Diagram displaying the procedure steps taken to produce and analyze the Misalignment Cases for each Aperture type.**

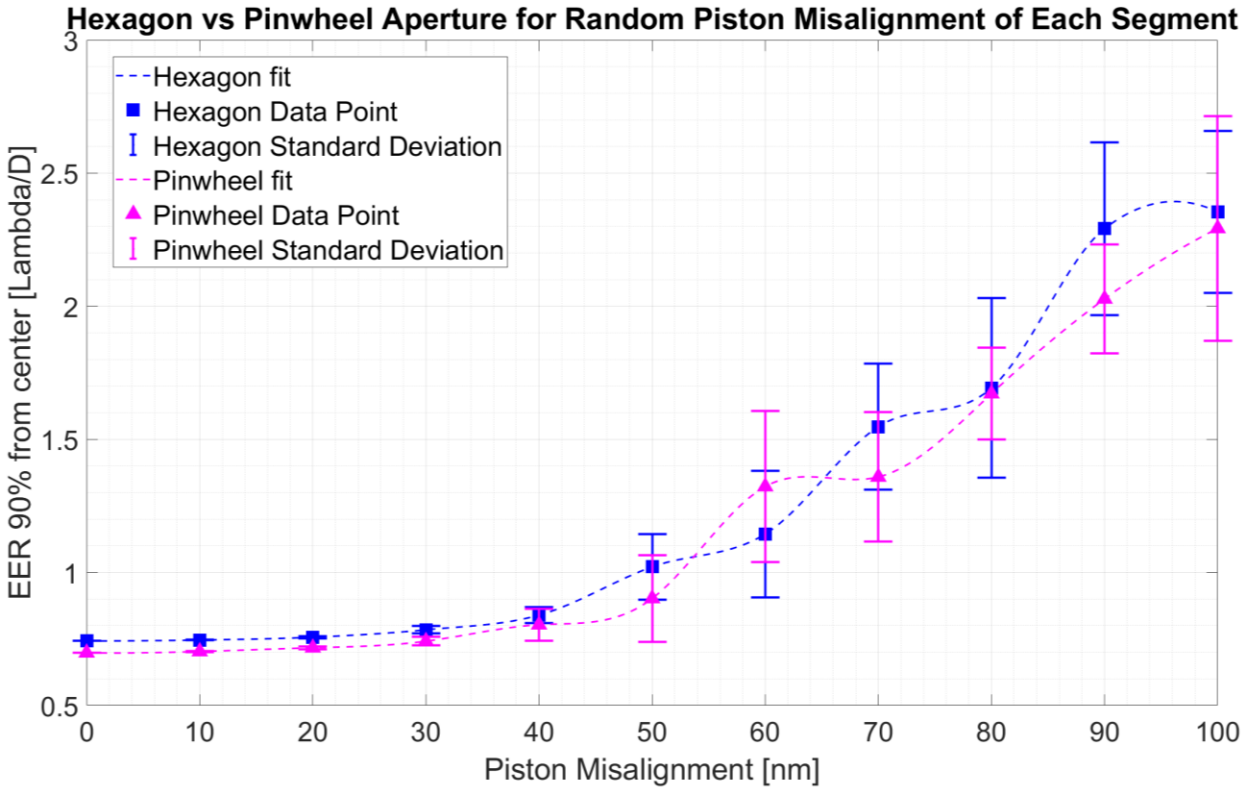


**Figure 20. Display of the EER values from the Monte Carlo analysis for each Aperture with random Piston Misalignment.**

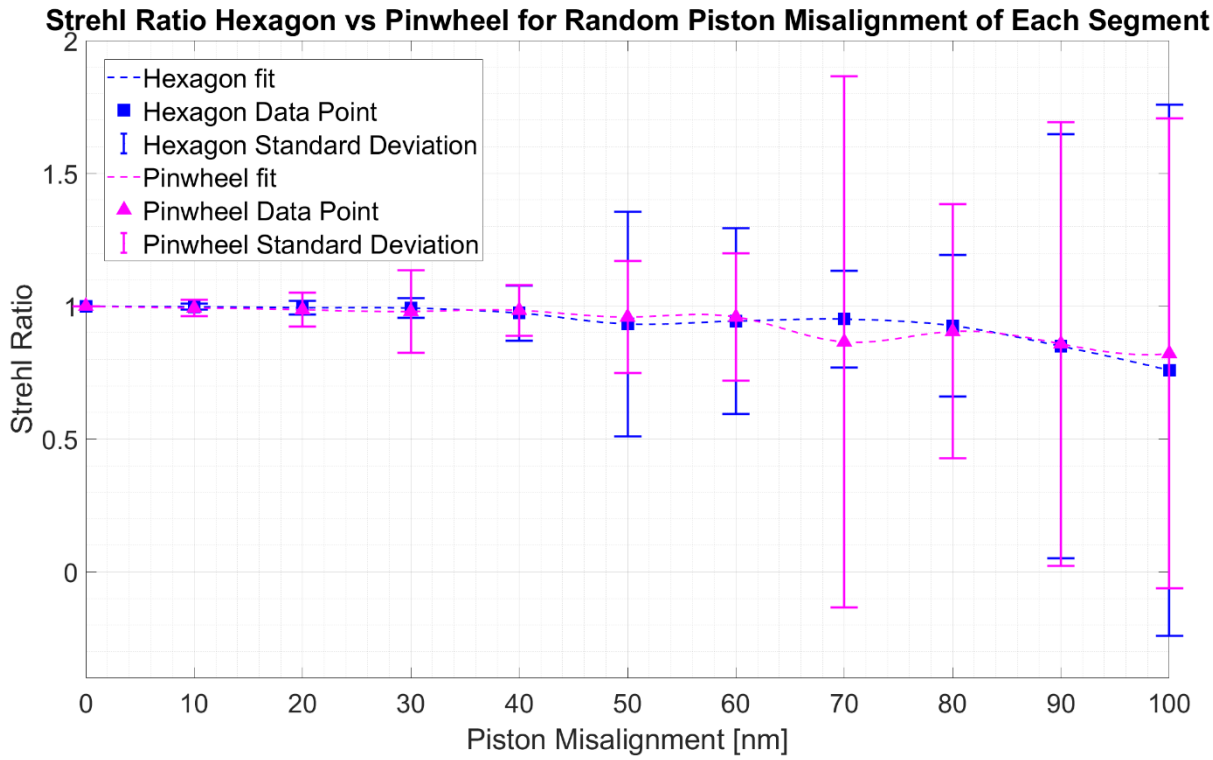


**Figure 21. Display of the Strehl Ratio values from the Monte Carlo analysis for each Aperture with random Piston Misalignment.**

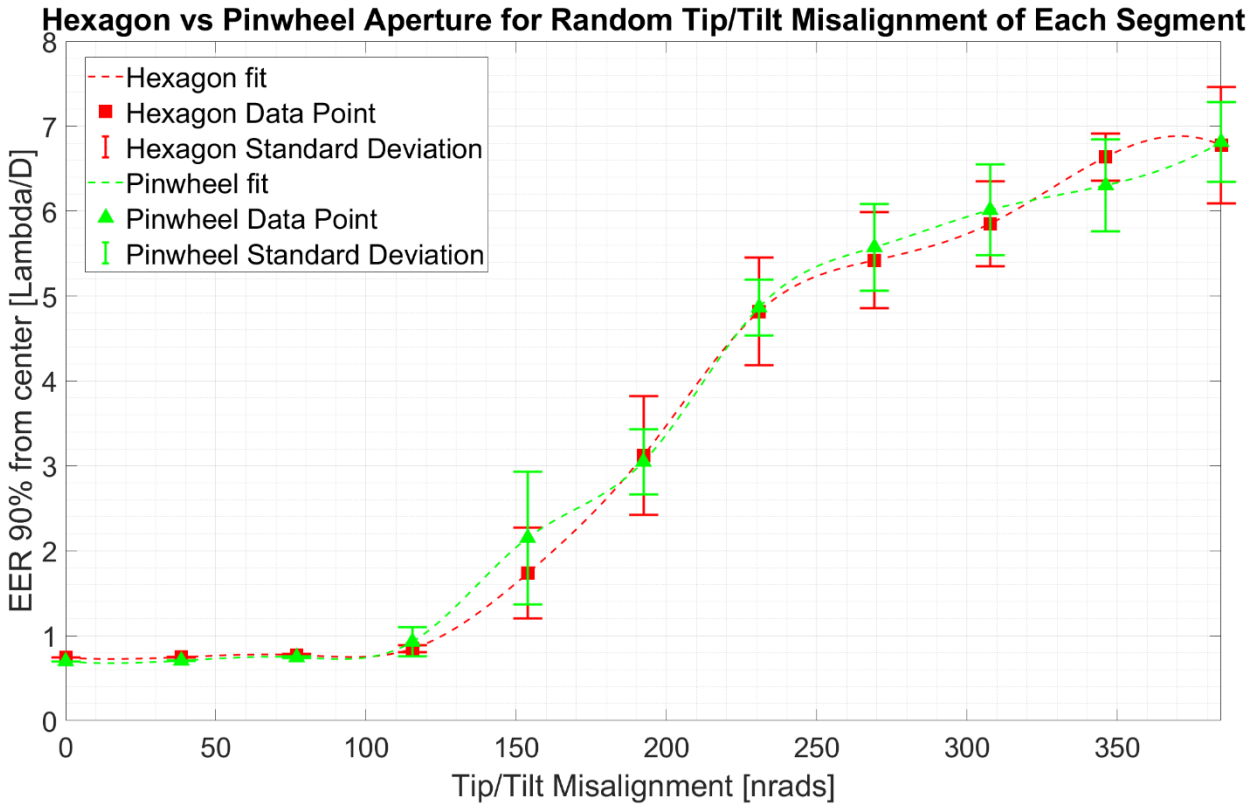


**Figure 22. Display of the EER values from the Monte Carlo analysis for each Aperture with random Tip/Tilt Misalignment.**

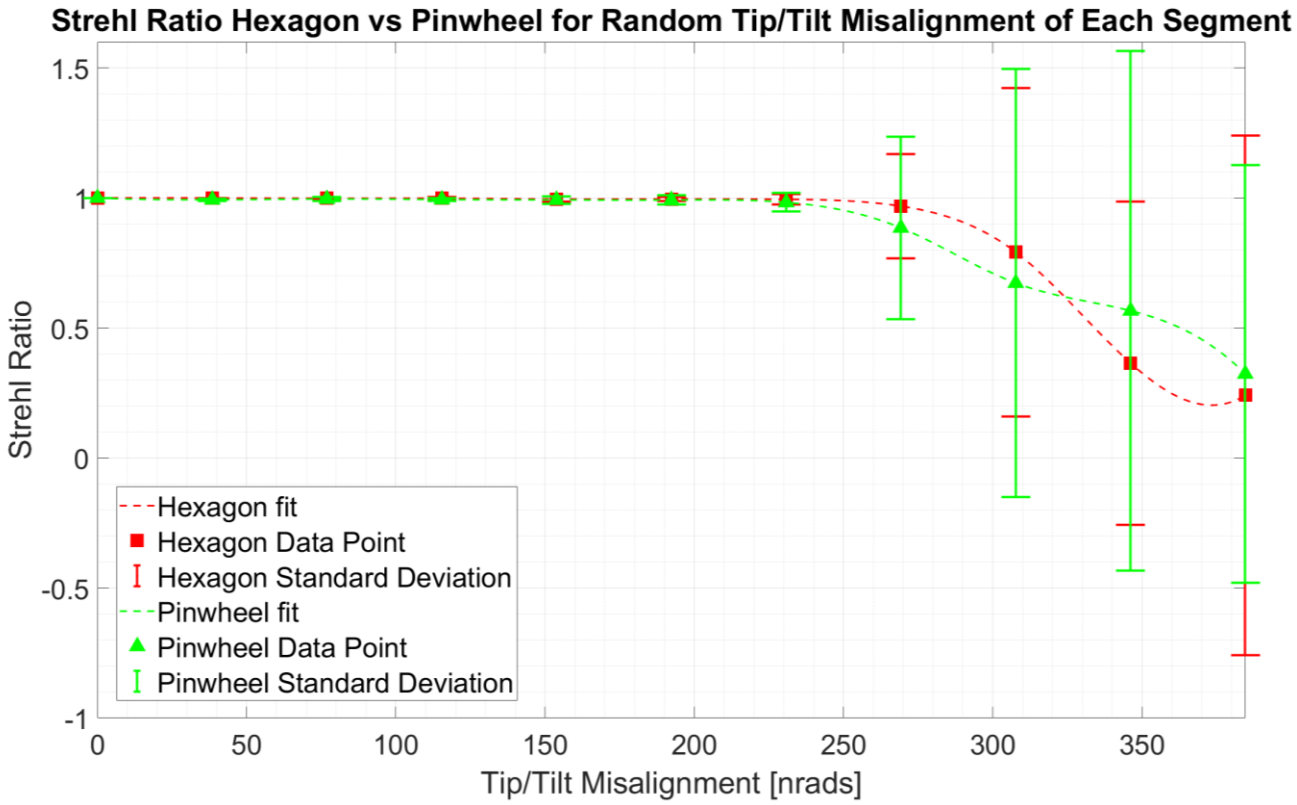


**Figure 23. Display of the Strehl Ratio values from the Monte Carlo analysis for each Aperture with random Tip/Tilt Misalignment.**

## 8. CONCLUSION

It was the hypothesis of this paper that the Pinwheel Aperture would be less sensitive to segment misalignments relative to the Hexagonal Aperture. This hypothesis was assumed due to the intentional topology of the Pinwheel Aperture. The topology was designed to fan out the diffraction spikes introduced by the edges of the segments. This fan out feature of the Pinwheel was thought to have further anti-aberration like qualities. The plots above containing the Monte Carlo Runs for the Misalignment cases are inconclusive. The two apertures seem to behave similarly when the Misalignments are introduced. A deeper dive into the Monte Carlo averages shows that the hypothesis was incorrect. The Pinwheel Aperture is more sensitive to Piston and Tip/Tilt Misalignment than the Hexagonal Aperture. The Hexagonal Aperture was less sensitive for most of the Piston data runs, and overall was 1.20% less sensitive than the Pinwheel Aperture. The Hexagonal Aperture was less sensitive for all of the Tip/Tilt data runs, and overall was 7.05% less sensitive than the Pinwheel Aperture. The final data comparisons can be seen in Table 4 and Table 5 below. The EER data was preferred over the Strehl data because the standard deviations were much smaller, indicating a more precise measurement for the final comparison.

| Table 4. Monte Carlo PISTON EER | | | | | | |
|---|---|---|---|---|---|---|
| [nm] | Hexagonal [λ/D] | X Ideal | % Diff. | Pinwheel [λ/D] | X Ideal | % Diff. |
| 0 | 0.7423 | | | 0.6979 | | |
| 10 | 0.7458 | **1.0047** | **0.22%** | 0.7027 | **1.0069** | |
| 20 | 0.7564 | **1.0190** | **0.76%** | 0.7166 | **1.0269** | |
| 30 | 0.7842 | **1.0565** | **0.55%** | 0.7414 | **1.0624** | |
| 40 | 0.8394 | **1.1309** | **1.75%** | 0.8033 | **1.1511** | |
| 50 | 1.0207 | **1.3751** | | 0.9019 | **1.2924** | **6.02%** |
| 60 | 1.1441 | **1.5414** | **18.65%** | 1.3223 | **1.8948** | |
| 70 | 1.5473 | **2.0845** | | 1.3584 | **1.9465** | **6.62%** |
| 80 | 1.6926 | **2.2803** | **4.79%** | 1.6714 | **2.3951** | |
| 90 | 2.2913 | **3.0868** | | 2.0274 | **2.9051** | **5.89%** |
| 100 | 2.3539 | **3.1712** | **3.45%** | 2.2922 | **3.2846** | |
| | **Total** | **17.7505** | **1.20%** | **Total** | **17.9657** | |

**Table 4. Summary of Monte Carlo analysis for Piston EER of each Aperture type.**

| Table 5. Monte Carlo TIP/TILT EER | | | | | | |
|---|---|---|---|---|---|---|
| [nrads] | Hexagonal [λ/D] | X Ideal | % Diff. | Pinwheel [λ/D] | X Ideal | % Diff. |
| 0 | 0.7423 | | | 0.6979 | | |
| 38.5 | 0.7477 | **1.0072** | **0.50%** | 0.7064 | **1.0123** | |
| 76.9 | 0.7738 | **1.0425** | **2.42%** | 0.7456 | **1.0684** | |
| 115.4 | 0.8464 | **1.1402** | **14.33%** | 0.9289 | **1.3310** | |
| 153.8 | 1.7354 | **2.3379** | **24.16%** | 2.1513 | **3.0827** | |
| 192.3 | 3.1211 | **4.2048** | **3.75%** | 3.0488 | **4.3687** | |
| 230.8 | 4.8188 | **6.4920** | **6.88%** | 4.8654 | **6.9718** | |
| 269.2 | 5.4207 | **7.3028** | **8.57%** | 5.5740 | **7.9871** | |
| 307.7 | 5.8525 | **7.8846** | **8.49%** | 6.0129 | **8.6161** | |
| 346.2 | 6.6380 | **8.9428** | **0.99%** | 6.3031 | **9.0320** | |
| 384.6 | 6.7743 | **9.1264** | **6.53%** | 6.8136 | **9.7635** | |
| | **Total** | **49.4811** | **7.05%** | **Total** | **53.2337** | |

**Table 5. Summary of Monte Carlo analysis for Tip/Tilt EER of each Aperture type.**

# APPENDIX

| Hexagonal: Piston EER DATA | | | | | | | | | | | | |
|---|---|---|---|---|---|---|---|---|---|---|---|---|
| | Aperture | Hex | Hex | Hex | Hex | Hex | Hex | Hex | Hex | Hex | Hex | Hex |
| | Misalignment Type | Ideal | Piston | Piston | Piston | Piston | Piston | Piston | Piston | Piston | Piston | Piston |
| | Piston [nm] | 0 | 10 | 20 | 30 | 40 | 50 | 60 | 70 | 80 | 90 | 100 |
| Data1 | Y (Lambda/D) | 0.742 | 0.745 | 0.760 | 0.789 | 0.860 | 1.156 | 0.999 | 1.191 | 2.083 | 2.392 | 2.212 |
| Data2 | Y (Lambda/D) | 0.742 | 0.745 | 0.765 | 0.796 | 0.838 | 1.113 | 1.034 | 1.721 | 1.700 | 2.701 | 2.348 |
| Data3 | Y (Lambda/D) | 0.742 | 0.748 | 0.754 | 0.775 | 0.830 | 0.963 | 1.475 | 1.799 | 1.759 | 1.740 | 2.148 |
| Data4 | Y (Lambda/D) | 0.742 | 0.747 | 0.754 | 0.775 | 0.829 | 1.027 | 0.918 | 1.199 | 1.648 | 2.082 | 2.475 |
| Data5 | Y (Lambda/D) | 0.742 | 0.746 | 0.755 | 0.791 | 0.818 | 1.017 | 1.201 | 1.650 | 0.941 | 2.739 | 2.512 |
| Data6 | Y (Lambda/D) | 0.742 | 0.745 | 0.754 | 0.780 | 0.853 | 1.197 | 0.949 | 1.302 | 1.910 | 2.408 | 2.869 |
| Data7 | Y (Lambda/D) | 0.742 | 0.745 | 0.758 | 0.815 | 0.819 | 1.103 | 1.457 | 1.719 | 1.515 | 2.470 | 2.027 |
| Data8 | Y (Lambda/D) | 0.742 | 0.744 | 0.750 | 0.766 | 0.809 | 0.807 | 1.024 | 1.695 | 1.628 | 1.925 | 1.879 |
| Data9 | Y (Lambda/D) | 0.742 | 0.746 | 0.757 | 0.780 | 0.827 | 0.899 | 0.911 | 1.464 | 2.150 | 2.097 | 2.348 |
| Data10 | Y (Lambda/D) | 0.742 | 0.748 | 0.756 | 0.775 | 0.911 | 0.925 | 1.473 | 1.731 | 1.591 | 2.358 | 2.721 |
| | Mean (Lambda/D) | 0.742275 | 0.745792 | 0.756398 | 0.784244 | 0.839426 | 1.020696 | 1.144127 | 1.547258 | 1.692600 | 2.291290 | 2.353919 |
| | Standard Deviation | 0.00000 | 0.00136 | 0.00398 | 0.01407 | 0.02943 | 0.12387 | 0.23808 | 0.23691 | 0.33776 | 0.32454 | 0.30483 |
| Hexagonal: Piston Strehl DATA | | | | | | | | | | | | |
| | Aperture | Hex | Hex | Hex | Hex | Hex | Hex | Hex | Hex | Hex | Hex | Hex |
| | Type | Ideal | Piston | Piston | Piston | Piston | Piston | Piston | Piston | Piston | Piston | Piston |
| | Piston [nm] | 0 | 10 | 20 | 30 | 40 | 50 | 60 | 70 | 80 | 90 | 100 |
| Data1 | Y (Strehl) | 255 | 255 | 251 | 252 | 251 | 239 | 202 | 250 | 249 | 235 | 135 |
| Data2 | Y (Strehl) | 255 | 254 | 254 | 253 | 248 | 198 | 236 | 235 | 230 | 252 | 234 |
| Data3 | Y (Strehl) | 255 | 254 | 254 | 250 | 249 | 243 | 253 | 231 | 245 | 188 | 229 |
| Data4 | Y (Strehl) | 255 | 254 | 254 | 253 | 249 | 255 | 249 | 244 | 227 | 254 | 107 |
| Data5 | Y (Strehl) | 255 | 255 | 253 | 255 | 253 | 245 | 235 | 232 | 245 | 203 | 180 |
| Data6 | Y (Strehl) | 255 | 254 | 255 | 252 | 252 | 236 | 248 | 253 | 211 | 198 | 195 |
| Data7 | Y (Strehl) | 255 | 255 | 255 | 253 | 254 | 243 | 252 | 239 | 241 | 253 | 251 |
| Data8 | Y (Strehl) | 255 | 255 | 254 | 254 | 244 | 255 | 248 | 252 | 231 | 237 | 216 |
| Data9 | Y (Strehl) | 255 | 255 | 253 | 255 | 245 | 212 | 251 | 247 | 235 | 200 | 196 |
| Data10 | Y (Strehl) | 255 | 254 | 253 | 255 | 239 | 253 | 233 | 243 | 248 | 146 | 192 |
| | Mean (Lambda/D) | 255.000000 | 254.500000 | 253.600000 | 253.200000 | 248.400000 | 237.900000 | 240.700000 | 242.600000 | 236.200000 | 216.600000 | 193.500000 |
| | Standard Deviation | 0.00000 | 0.52705 | 1.17379 | 1.61933 | 4.62361 | 18.80573 | 15.53526 | 8.09938 | 11.86779 | 35.49710 | 44.48533 |

**Table A-1. Hexagonal Aperture Data output for the Monte Carlo runs of random Piston Misalignment.**

| Pinwheel: Piston EER DATA | | | | | | | | | | | | |
|---|---|---|---|---|---|---|---|---|---|---|---|---|
| | Aperture | Pinwheel | Pinwheel | Pinwheel | Pinwheel | Pinwheel | Pinwheel | Pinwheel | Pinwheel | Pinwheel | Pinwheel | Pinwheel |
| | Misalignmetn Type | Ideal | Piston | Piston | Piston | Piston | Piston | Piston | Piston | Piston | Piston | Piston |
| | Piston [nm] | 0 | 10 | 20 | 30 | 40 | 50 | 60 | 70 | 80 | 90 | 100 |
| Data1 | Y (Lambda/D) | 0.698 | 0.704 | 0.712 | 0.740 | 0.956 | 0.831 | 1.526 | 1.088 | 1.692 | 2.066 | 2.126 |
| Data2 | Y (Lambda/D) | 0.698 | 0.706 | 0.723 | 0.737 | 0.769 | 0.787 | 0.866 | 1.589 | 1.406 | 2.354 | 2.638 |
| Data3 | Y (Lambda/D) | 0.698 | 0.704 | 0.710 | 0.756 | 0.751 | 0.822 | 1.663 | 1.554 | 1.738 | 2.094 | 2.195 |
| Data4 | Y (Lambda/D) | 0.698 | 0.699 | 0.717 | 0.718 | 0.779 | 1.062 | 1.515 | 1.426 | 1.563 | 1.983 | 2.342 |
| Data5 | Y (Lambda/D) | 0.698 | 0.702 | 0.725 | 0.739 | 0.756 | 0.855 | 1.534 | 1.682 | 1.689 | 1.944 | 3.069 |
| Data6 | Y (Lambda/D) | 0.698 | 0.705 | 0.717 | 0.723 | 0.768 | 0.835 | 1.292 | 1.331 | 1.665 | 2.071 | 2.672 |
| Data7 | Y (Lambda/D) | 0.698 | 0.702 | 0.716 | 0.772 | 0.807 | 0.811 | 1.496 | 1.310 | 1.595 | 1.880 | 1.539 |
| Data8 | Y (Lambda/D) | 0.698 | 0.699 | 0.717 | 0.742 | 0.803 | 1.306 | 0.845 | 0.886 | 1.687 | 1.602 | 2.109 |
| Data9 | Y (Lambda/D) | 0.698 | 0.705 | 0.714 | 0.750 | 0.821 | 0.909 | 1.307 | 1.486 | 1.597 | 2.030 | 2.240 |
| Data10 | Y (Lambda/D) | 0.698 | 0.702 | 0.716 | 0.736 | 0.823 | 0.801 | 1.177 | 1.232 | 2.083 | 2.250 | 1.992 |
| | Mean (Lambda/D) | 0.697866 | 0.702707 | 0.716611 | 0.741422 | 0.803279 | 0.901907 | 1.322288 | 1.358417 | 1.671433 | 2.027382 | 2.292186 |
| | Standard Deviation | 0.00000 | 0.00246 | 0.00469 | 0.01569 | 0.05969 | 0.16275 | 0.28448 | 0.24310 | 0.17263 | 0.20436 | 0.42179 |
| Pinwheel: Piston Strehl DATA | | | | | | | | | | | | |
| | Aperture | Pinwheel | Pinwheel | Pinwheel | Pinwheel | Pinwheel | Pinwheel | Pinwheel | Pinwheel | Pinwheel | Pinwheel | Pinwheel |
| | Type | Ideal | Piston | Piston | Piston | Piston | Piston | Piston | Piston | Piston | Piston | Piston |
| | Piston [nm] | 0 | 10 | 20 | 30 | 40 | 50 | 60 | 70 | 80 | 90 | 100 |
| Data1 | Y (Strehl) | 255 | 252 | 255 | 250 | 255 | 253 | 249 | 215 | 232 | 250 | 254 |
| Data2 | Y (Strehl) | 255 | 252 | 250 | 253 | 251 | 249 | 251 | 253 | 249 | 229 | 138 |
| Data3 | Y (Strehl) | 255 | 252 | 253 | 253 | 250 | 254 | 252 | 231 | 219 | 157 | 223 |
| Data4 | Y (Strehl) | 255 | 255 | 252 | 254 | 254 | 231 | 248 | 247 | 225 | 243 | 188 |
| Data5 | Y (Strehl) | 255 | 253 | 247 | 250 | 254 | 243 | 252 | 222 | 253 | 237 | 194 |
| Data6 | Y (Strehl) | 255 | 253 | 249 | 255 | 254 | 243 | 241 | 216 | 198 | 215 | 200 |
| Data7 | Y (Strehl) | 255 | 254 | 253 | 249 | 252 | 252 | 254 | 127 | 213 | 166 | 233 |
| Data8 | Y (Strehl) | 255 | 254 | 252 | 251 | 245 | 234 | 238 | 246 | 251 | 224 | 234 |
| Data9 | Y (Strehl) | 255 | 253 | 254 | 234 | 250 | 248 | 234 | 196 | 243 | 237 | 195 |
| Data10 | Y (Strehl) | 255 | 255 | 251 | 250 | 245 | 239 | 227 | 254 | 225 | 230 | 237 |
| | Mean (Lambda/D) | 255.000000 | 253.300000 | 251.600000 | 249.900000 | 251.000000 | 244.600000 | 244.600000 | 220.700000 | 230.800000 | 218.800000 | 209.600000 |
| | Standard Deviation | 0.00000 | 1.15950 | 2.41293 | 5.93390 | 3.62093 | 8.01665 | 9.11897 | 38.05858 | 18.20134 | 31.79727 | 33.64257 |

**Table A-2. Pinwheel Aperture Data output for the Monte Carlo runs of random Piston Misalignment.**

| Hexagonal: Tip/Tilt EER DATA | | | | | | | | | | | | |
|---|---|---|---|---|---|---|---|---|---|---|---|---|
| | Aperture | Hex | Hex | Hex | Hex | Hex | Hex | Hex | Hex | Hex | Hex | Hex |
| | Type | Ideal | Tip/Tilt | Tip/Tilt | Tip/Tilt | Tip/Tilt | Tip/Tilt | Tip/Tilt | Tip/Tilt | Tip/Tilt | Tip/Tilt | Tip/Tilt |
| | TT in [nrads] | 0 | 38.5 | 76.9 | 115.4 | 153.8 | 192.3 | 230.8 | 269.2 | 307.7 | 346.2 | 384.6 |
| Data1 | Y (Lambda/D) | 0.742 | 0.749 | 0.763 | 0.818 | 1.723 | 2.625 | 4.121 | 4.776 | 5.211 | 7.101 | 6.794 |
| Data2 | Y (Lambda/D) | 0.742 | 0.747 | 0.794 | 0.824 | 2.675 | 2.909 | 5.276 | 5.039 | 5.801 | 6.585 | 6.233 |
| Data3 | Y (Lambda/D) | 0.742 | 0.746 | 0.772 | 0.833 | 1.107 | 3.469 | 5.473 | 6.001 | 6.540 | 6.941 | 7.153 |
| Data4 | Y (Lambda/D) | 0.742 | 0.746 | 0.769 | 0.846 | 1.298 | 3.308 | 5.353 | 5.636 | 6.055 | 6.222 | 6.999 |
| Data5 | Y (Lambda/D) | 0.742 | 0.748 | 0.780 | 0.936 | 2.335 | 2.045 | 4.835 | 4.895 | 6.537 | 6.953 | 6.840 |
| Data6 | Y (Lambda/D) | 0.742 | 0.747 | 0.769 | 0.804 | 1.592 | 2.127 | 5.428 | 6.316 | 5.500 | 6.480 | 6.921 |
| Data7 | Y (Lambda/D) | 0.742 | 0.747 | 0.768 | 0.879 | 1.970 | 4.093 | 4.241 | 4.596 | 5.954 | 6.396 | 7.276 |
| Data8 | Y (Lambda/D) | 0.742 | 0.749 | 0.780 | 0.886 | 2.071 | 3.626 | 5.360 | 5.502 | 5.862 | 6.480 | 7.147 |
| Data9 | Y (Lambda/D) | 0.742 | 0.749 | 0.774 | 0.807 | 1.574 | 3.893 | 4.076 | 5.702 | 5.017 | 6.648 | 5.038 |
| Data10 | Y (Lambda/D) | 0.742 | 0.748 | 0.768 | 0.830 | 1.007 | 3.117 | 4.025 | 5.742 | 6.047 | 6.573 | 7.342 |
| | Mean (Lambda/D) | 0.742275 | 0.747651 | 0.773829 | 0.846360 | 1.735402 | 3.121112 | 4.818815 | 5.420653 | 5.852522 | 6.638003 | 6.774275 |
| | Standard Deviation | 0.00000 | 0.00112 | 0.00908 | 0.04179 | 0.53470 | 0.69810 | 0.63145 | 0.56683 | 0.50198 | 0.27785 | 0.68626 |
| Hexagonal: Tip/Tilt STREHL DATA | | | | | | | | | | | | |
| | Aperture | Hex | Hex | Hex | Hex | Hex | Hex | Hex | Hex | Hex | Hex | Hex |
| | Type | Ideal | Tip/Tilt | Tip/Tilt | Tip/Tilt | Tip/Tilt | Tip/Tilt | Tip/Tilt | Tip/Tilt | Tip/Tilt | Tip/Tilt | Tip/Tilt |
| | TT in [nrads] | 0 | 38.5 | 76.9 | 115.4 | 153.8 | 192.3 | 230.8 | 269.2 | 307.7 | 346.2 | 384.6 |
| Data1 | Y (Strehl) | 255 | 255 | 255 | 255 | 254 | 254 | 255 | 255 | 254 | 0 | 16 |
| Data2 | Y (Strehl) | 255 | 255 | 255 | 255 | 253 | 255 | 254 | 252 | 190 | 118 | 253 |
| Data3 | Y (Strehl) | 255 | 255 | 255 | 255 | 254 | 253 | 254 | 255 | 75 | 73 | 9 |
| Data4 | Y (Strehl) | 255 | 255 | 254 | 255 | 254 | 254 | 255 | 254 | 251 | 206 | 0 |
| Data5 | Y (Strehl) | 255 | 255 | 254 | 254 | 255 | 255 | 255 | 251 | 128 | 28 | 34 |
| Data6 | Y (Strehl) | 255 | 255 | 254 | 255 | 254 | 253 | 254 | 189 | 251 | 72 | 8 |
| Data7 | Y (Strehl) | 255 | 255 | 255 | 255 | 255 | 255 | 253 | 252 | 255 | 45 | 10 |
| Data8 | Y (Strehl) | 255 | 255 | 255 | 254 | 252 | 253 | 248 | 254 | 204 | 166 | 32 |
| Data9 | Y (Strehl) | 255 | 255 | 255 | 254 | 254 | 254 | 255 | 255 | 255 | 127 | 253 |
| Data10 | Y (Strehl) | 255 | 255 | 255 | 255 | 255 | 254 | 254 | 253 | 156 | 95 | 0 |
| | Mean (Lambda/D) | 255.000000 | 255.000000 | 254.700000 | 254.700000 | 254.000000 | 254.000000 | 253.700000 | 247.000000 | 201.900000 | 93.000000 | 61.500000 |
| | Standard Deviation | 0.00000 | 0.00000 | 0.48305 | 0.48305 | 0.94281 | 0.81650 | 2.11082 | 20.42874 | 64.11179 | 63.15941 | 101.58549 |

**Table A-3. Hexagonal Aperture Data output for the Monte Carlo runs of random Tip/Tilt Misalignment.**

| Pinwheel: Tip/Tilt EER DATA | | | | | | | | | | | | |
|---|---|---|---|---|---|---|---|---|---|---|---|---|
| | Aperture | Pinwheel | Pinwheel | Pinwheel | Pinwheel | Pinwheel | Pinwheel | Pinwheel | Pinwheel | Pinwheel | Pinwheel | Pinwheel |
| | Type | Ideal | Tip/Tilt | Tip/Tilt | Tip/Tilt | Tip/Tilt | Tip/Tilt | Tip/Tilt | Tip/Tilt | Tip/Tilt | Tip/Tilt | Tip/Tilt |
| | TT in [nrads] | 0 | 38.5 | 76.9 | 115.4 | 153.8 | 192.3 | 230.8 | 269.2 | 307.7 | 346.2 | 384.6 |
| Data1 | Y (Lambda/D) | 0.698 | 0.705 | 0.752 | 0.810 | 1.476 | 3.512 | 4.839 | 5.537 | 6.726 | 5.981 | 6.213 |
| Data2 | Y (Lambda/D) | 0.698 | 0.707 | 0.740 | 0.870 | 1.787 | 2.677 | 4.461 | 6.123 | 5.800 | 5.767 | 7.385 |
| Data3 | Y (Lambda/D) | 0.698 | 0.704 | 0.757 | 0.805 | 1.896 | 2.737 | 5.467 | 5.057 | 6.125 | 6.263 | 6.978 |
| Data4 | Y (Lambda/D) | 0.698 | 0.707 | 0.758 | 0.853 | 1.411 | 3.260 | 5.098 | 5.221 | 5.299 | 6.802 | 7.064 |
| Data5 | Y (Lambda/D) | 0.698 | 0.706 | 0.748 | 1.242 | 1.730 | 3.720 | 4.488 | 5.782 | 5.355 | 6.614 | 6.739 |
| Data6 | Y (Lambda/D) | 0.698 | 0.705 | 0.740 | 0.837 | 2.334 | 2.470 | 4.980 | 6.353 | 5.595 | 7.043 | 6.683 |
| Data7 | Y (Lambda/D) | 0.698 | 0.706 | 0.751 | 0.793 | 3.309 | 3.092 | 4.749 | 4.629 | 6.199 | 7.053 | 7.239 |
| Data8 | Y (Lambda/D) | 0.698 | 0.710 | 0.741 | 0.957 | 3.424 | 2.898 | 4.471 | 5.849 | 5.757 | 5.694 | 5.871 |
| Data9 | Y (Lambda/D) | 0.698 | 0.708 | 0.735 | 0.893 | 1.323 | 3.186 | 5.095 | 5.503 | 6.555 | 5.651 | 7.136 |
| Data10 | Y (Lambda/D) | 0.698 | 0.707 | 0.733 | 1.229 | 2.823 | 2.935 | 5.007 | 5.686 | 6.718 | 6.164 | 6.830 |
| | Mean (Lambda/D) | 0.6978663 | 0.7064400 | 0.7456007 | 0.9288747 | 2.1513201 | 3.0487791 | 4.8654095 | 5.5739531 | 6.0129048 | 6.3031111 | 6.8136131 |
| | Standard Deviation | 0.0000000 | 0.0018504 | 0.0090356 | 0.1685473 | 0.7824688 | 0.3854179 | 0.3296563 | 0.5088800 | 0.5348332 | 0.5440773 | 0.4682640 |
| Pinwheel: Tip/Tilt STREHL DATA | | | | | | | | | | | | |
| | Aperture | Pinwheel | Pinwheel | Pinwheel | Pinwheel | Pinwheel | Pinwheel | Pinwheel | Pinwheel | Pinwheel | Pinwheel | Pinwheel |
| | Type | Ideal | Tip/Tilt | Tip/Tilt | Tip/Tilt | Tip/Tilt | Tip/Tilt | Tip/Tilt | Tip/Tilt | Tip/Tilt | Tip/Tilt | Tip/Tilt |
| | TT in [nrads] | 0 | 38.5 | 76.9 | 115.4 | 153.8 | 192.3 | 230.8 | 269.2 | 307.7 | 346.2 | 384.6 |
| Data1 | Y (Strehl) | 255 | 254 | 254 | 254 | 253 | 254 | 255 | 253 | 52 | 211 | 136 |
| Data2 | Y (Strehl) | 255 | 254 | 253 | 253 | 253 | 255 | 255 | 150 | 253 | 249 | 6 |
| Data3 | Y (Strehl) | 255 | 254 | 253 | 254 | 255 | 254 | 246 | 251 | 237 | 142 | 41 |
| Data4 | Y (Strehl) | 255 | 253 | 253 | 254 | 254 | 250 | 251 | 244 | 254 | 22 | 9 |
| Data5 | Y (Strehl) | 255 | 253 | 255 | 253 | 251 | 250 | 254 | 224 | 244 | 116 | 72 |
| Data6 | Y (Strehl) | 255 | 253 | 255 | 254 | 252 | 255 | 254 | 177 | 231 | 1 | 131 |
| Data7 | Y (Strehl) | 255 | 253 | 254 | 253 | 251 | 252 | 250 | 254 | 180 | 12 | 4 |
| Data8 | Y (Strehl) | 255 | 253 | 254 | 253 | 255 | 253 | 246 | 214 | 121 | 242 | 255 |
| Data9 | Y (Strehl) | 255 | 253 | 254 | 254 | 254 | 253 | 248 | 243 | 78 | 255 | 30 |
| Data10 | Y (Strehl) | 255 | 253 | 255 | 253 | 253 | 254 | 248 | 247 | 66 | 194 | 141 |
| | Mean (Lambda/D) | 255.000000 | 253.300000 | 254.000000 | 253.500000 | 253.100000 | 253.000000 | 250.700000 | 225.700000 | 171.600000 | 144.400000 | 82.500000 |
| | Standard Deviation | 0.00000000 | 0.48304589 | 0.81649658 | 0.52704628 | 1.44913767 | 1.82574186 | 3.62246080 | 35.77103111 | 83.87185993 | 101.91630553 | 81.92035427 |

**Table A-4. Pinwheel Aperture Data output for the Monte Carlo runs of random Tip/Tilt Misalignment**

| Tip/Tilt Values | |
|---|---|
| nm | nano-radians |
| 25 | 38.46153846153840 |
| 50 | 76.92307692307680 |
| 75 | 115.38461538461500 |
| 100 | 153.84615384615300 |
| 125 | 192.30769230769000 |
| 150 | 230.76923076922700 |
| 175 | 269.23076923076300 |
| 200 | 307.69230769229800 |
| 225 | 346.15384615383200 |
| 250 | 384.61538461536600 |
| 3191 | 4909.23076919133000 |

**Table A-5. Tip/Tilt values converted to input angle.**

## REFERENCES


1. Wall, W. (2018). Astronomy as a Science in Need of a Tool. In: A History of Optical Telescopes in Astronomy. Historical & Cultural Astronomy. Springer, Cham. https://doi-org.ezproxy4.library.arizona.edu/10.1007/978-3-319-99088-0_1

2. Goodman, Joseph W. *Introduction to Fourier Optics*. Fourth ed. 2017. Print.

3. Oswalt, Terry D, and Ian S McLean. Planets, Stars and Stellar Systems, Volume 1. Dordrecht: Springer Netherlands, 2013. Web.

4. Stahl, H. Philip. "JWST Primary Mirror Technology Development Lessons Learned." Proceedings of SPIE 7796.1 (2010): 779604-79608. Web.

5. Feng, Yi-Ting, Jaren Nicholas Ashcraft, James B Breckinridge, James E Harvey, Ewan S Douglas, Heejoo Choi, Charles Lillie, Tony Hull, and Dae Wook Kim. "Topological Pupil Segmentation and Point Spread Function Analysis for Large Aperture Imaging Systems." 11568 (2020): 115680I-15680I-13. Web.

6. Yaitskova, Natalia, Kjetil Dohlen, and Philippe Dierickx. "Analytical Study of Diffraction Effects in Extremely Large Segmented Telescopes." *Journal of the Optical Society of America. A, Optics, Image Science, and Vision* 20.8 (2003): 1563-575. Web.

7. Derby, K.Z, J.B Breckinridge, J.E Harvey, T. Hull, C.F Lillie, J.N Ashcraft, H. Choi, E.S Douglas, D. Kim, and University of Arizona Wyant College of Optical Sciences. *Curved Primary Aperture Segmentation Enabling a Robust Quasi-Airy Pattern Point Spread Function* (2022): Proceedings of SPIE - The International Society for Optical Engineering. Web.

8. Harvey, James E, James B Breckinridge, Ryan G Irvin, and Richard N Pfisterer. "Novel Designs for Minimizing Diffraction Effects of Large Segmented Mirror Telescopes." 10745 (2018): 107450L-07450L-14. Web.

9. Yaitskova, Natalia, and Kjetil Dohlen. "Tip-tilt Error for Extremely Large Segmented Telescopes: Detailed Theoretical Point-spread-function Analysis and Numerical Simulation Results." *Journal of the Optical Society of America. A, Optics, Image Science, and Vision* 19.7 (2002): 1274-285. Web.

10. Richter, J. L. "Spider Diffraction: A Comparison of Curved and Straight Legs." *Applied Optics* 23.12 (1984): 1907-913. Web.

11. Breckinridge, James B, James E Harvey, Karlton Crabtree, and Tony Hull. "Exoplanet Telescope Diffracted Light Minimized: The Pinwheel-pupil Solution." 10698 (2018): 106981P-06981P-10. Web.

12. Milster, D. Tom, Chapter 5 Scalar Diffraction. 2019.

13. Kreyszig, Norminton, Kreyszig, Herbert, and Norminton, E. J. *Advanced Engineering Mathematics*. 10th ed. 2011. Web.

14. Nichols, Jonathan M, Ronald G Driggers, and Melvin H Friedman. *Introduction to Infrared and Electro-Optical Systems, Second Edition*. 2nd ed. Boston, Mass.: Artech House, 2012. Artech Optoelectronics and Applied Sciences. Web.

15. Lightsey, Paul A, and Michael Chrisp. "Image Quality for Large Segmented Space Telescopes." *Proceedings of SPIE* 4850.1 (2003): 453-60. Web.

16. Por, Emiel H, Sebastiaan Y Haffert, Vikram M Radhakrishnan, David S Doelman, Maaike Van Kooten, and Steven P Bos. "High Contrast Imaging for Python (HCIPy): An Open-source Adaptive Optics and Coronagraph Simulator." 10703 (2018): 1070342-070342-14. Web.